MICROCOPY RESOLUTION TEST CHART

NATIONAL BUREAU OF STANDARDS 1964 A

⑫ **LEVEL** Ⅱ A

ASL-CR-80-0043-2

AD

OPTICAL AND FLUID DYNAMIC PROPERTIES
OF EXPLOSION - PRODUCED DUST CLOUDS

ADA085930

MAY 1980

Prepared by
JOHN F. EBERSOLE
ROBERTO VAGLIO-LAURIN
DAVID S. DVORE

AERODYNE RESEARCH, INC.
BEDFORD RESEARCH PARK
CROSBY DRIVE
BEDFORD, MA 01730

DTIC
S ELECTE D
JUN 23 1980
B

DOC FILE COPY

US Army Electronics Research and Development Command
ATMOSPHERIC SCIENCES LABORATORY
White Sands Missile Range, NM 88002

80 6 18 0 41

NOTICES

Disclaimers

The findings in this report are not to be construed as an
official Department of the Army position, unless so desig-
nated by other authorized documents.

The citation of trade names and names of manufacturers in
this report is not to be construed as official Government
indorsement or approval of commercial products or services
referenced herein.

Disposition

Destroy this report when it is no longer needed. Do not
return it to the originator.

REPORT DOCUMENTATION PAGE	READ INSTRUCTIONS BEFORE COMPLETING FORM

1. REPORT NUMBER	2. GOVT ACCESSION NO.	3. RECIPIENT'S CATALOG NUMBER
ASL-CR-80-0043-2	ADA 085 930	

4. TITLE (and Subtitle)	5. TYPE OF REPORT & PERIOD COVERED
OPTICAL AND FLUID DYNAMIC PROPERTIES OF EXPLOSION-PRODUCED DUST CLOUDS	Final Technical Report, June 1979 — September 1979
	6. PERFORMING ORG. REPORT NUMBER
	ARI-RR-181.1

7. AUTHOR(s)	8. CONTRACT OR GRANT NUMBER(s)
John F. Ebersole, Roberto Vaglio-Laurin, David S. Dvore	DAAK20-79-Q-0043

9. PERFORMING ORGANIZATION NAME AND ADDRESS	10. PROGRAM ELEMENT, PROJECT, TASK AREA & WORK UNIT NUMBERS
Aerodyne Research, Inc. Bedford Research Park, Crosby Drive Bedford, MA 01730	

11. CONTROLLING OFFICE NAME AND ADDRESS	12. REPORT DATE
Mr. George Haber Electronics Warfare Laboratory Ft. Monmouth, NJ 07703	May 1980
	13. NUMBER OF PAGES
	73

14. MONITORING AGENCY NAME & ADDRESS(if different from Controlling Office)	15. SECURITY CLASS (of this report)
Dr. Louis Duncan Atmospheric Sciences Laboratory White Sands Missile Range, NM	Unclassified
	15a. DECLASSIFICATION/DOWNGRADING SCHEDULE

16. DISTRIBUTION STATEMENT (of this Report)

Approved for public release; distribution unlimited

17. DISTRIBUTION STATEMENT (of the abstract entered in Block 20, if different from Report)

18. SUPPLEMENTARY NOTES

19. KEY WORDS (Continue on reverse side if necessary and identify by block number)

Dust	Obscuration	MM-Wave	Gravitational Settling
Aerosol	Transmission	Atmospheric Diffusion	tling
Explosions	Visible	Wind Shear	DIRT I Test
Artillery	Infrared	Buoyancy	Graf II Test

20. ABSTRACT (Continue on reverse side if necessary and identify by block number)

A model (DIRTRAN) descriptive of time/space dependent optical properties of explosion-generated dust clouds has been developed. This model includes three components: a dust source term, atmospheric diffusion, and optical transmission. Data analysis indicates that for a given soil, the greatest uncertainties lie in the determination of soil comminution/agglomeration under the dynamic loading produced by explosions. When an empirical parameter

DD FORM 1473 EDITION OF 1 NOV 65 IS OBSOLETE
1 JAN 73
S/N 0102-LF-014-6601

descriptive of this effect is employed, the model predicts cloud optical
properties which compare favorably with experiments under a variety of
explosion patterns, charge types, and atmospheric conditions. A computer
code (DIRTRAN-I) which embodies this model has been delivered to the Army
Atmospheric Sciences Laboratory for inclusion in the Electro-Optics Systems
Atmospheric Effects Library.

ACKNOWLEDGEMENTS

3

TABLE OF CONTENTS

LIST OF ILLUSTRATIONS

1. INTRODUCTION

A knowledge of the fluid dynamic and optical properties of explosion-generated dust clouds is a prerequisite to the realistic assessment of electro-optical (EO) system battlefield performance degradation. Aerodyne Research, Inc. has constructed a model -- DIRTRAN (Disturbed Infrared Transmission) -- which describes those time/space dependent cloud properties as a function of explosive charge, soil characteristics, atmospheric conditions, and EO system operating wavelengths. This report describes the structure and features of the components of the model, presents selected results of its validation against photographic and optical data obtained in the DIRT I and Graf II-Winter field trials, and discusses issues which must be resolved by future theoretical and experimental studies.

The components of the model are discussed in sequence, namely: (1) the dust source term and initial cloud formation; (2) the diffusion of the initial cloud under the action of buoyant-rise/wind-driven diffusion and gravitational settling of the dust particles; (3) the time dependent extinction of visible, infrared, and millimeter wavelength radiation by the dust cloud along pre-scribed lines of sight.

A computer code -- DIRTRAN-I -- which embodies the DIRTRAN model and is compatible with the Electro Optics System Atmospheric Effects Library (EO-SAEL), is described in Ref. 1 and has been delivered to the Army Atmospheric Sciences Laboratory.

Preceding Page Blank -

2. CHARACTERISTICS OF DUST SOURCE TERM AND INITIAL DUST CLOUDS

2.1 Airborne Dust Source

The quantitative determination of the aerosol source term depends on two major steps: (1) the mass of aerosol injected into the atmosphere; (2) the distribution function of that mass as a function of dust particle size. The practical significance of accurate analyses is illustrated in Figs. 1 and 2.

Figure 1 shows the results of transmission tests in the 8-12 μm band performed by the Army Night Vision & Electro-Optics Laboratory (NV&EOL), Ft. Belvoir, VA. This test -- known as TAPATS (Threat Artillery Preparation Against Tank Sights) was conducted in July 1978 at Ft. Knox, Ky. The Transmission data shown are the results of viewing through a 155 mm HE barrage of intensity 0.7 rounds/km/sec. Notable in the figure is the fact that from the first-round impact to several tens of seconds after the barrage ended, the transmission was essentially zero (at best 4% at regular intervals). In Fig. 2 is plotted the transmission during a barrage conducted at Grafenwohr, Germany in November 1978 by NV&EOL. In this case, the barrage had an intensity of 1.5 rounds/km/sec. Here, attenuation due to background fog (as determined prior to the barrage) has been removed from the transmission data so that what is shown in the figure is strictly the loss in transmission to the barrage. It is evident from the figure that the transmission was considerably in excess of 20 to 40% for several tens of seconds at several different times during the barrage. We point out that relative to the Graf II case, the TAPATS test had

    a. Comparable soil moisture content

    b. Half the barrage intensity

    c. 50% greater windspeed

    d. Greater atmospheric diffusivity (approximately Pasquill Category B versus C for Graf II).

10

(Ft. Knox, Ky.)

WAVELENGTH BAND: 8 - 12 μM
ARTILLERY: 155 MM HE
BARRAGE: 0.7 ROUNDS/KM/SEC
IMPACT AREA: 100 M x 300 M
ATMOSPHERE: PASQUILL CATEGORY B
WINDSPEED· 4.5 KNOTS
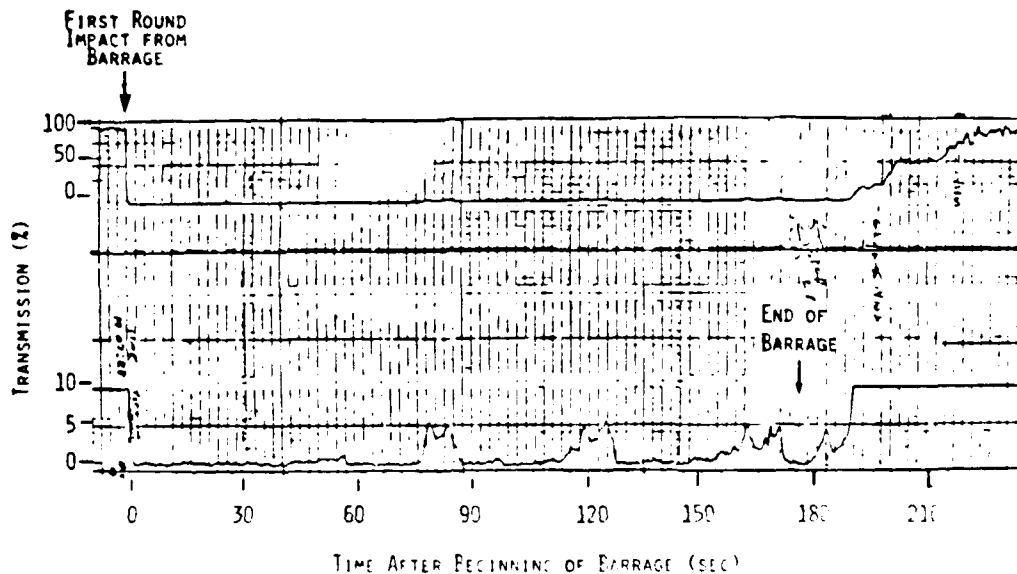
Figure 1. Transmission in the 8-12 μm Band During a 155 mm HE Barrage at Ft. Knox, Ky. For this barrage intensity and atmospheric condition, essentially zero transmission (at most 4% at regular intervals) was observed for the duration of the barrage and several tens of seconds after it. (Data from the TAPATS test conducted by the Night Vision & Electro-Optics Laboratory, Ft. Belvoir, VA, July 1978.)

11

GRAF II
RELATIVE TRANSMISSION
(BACKGROUND FOG AND AEROSOL ATTENUATION REMOVED)
10 NOVEMBER 1978
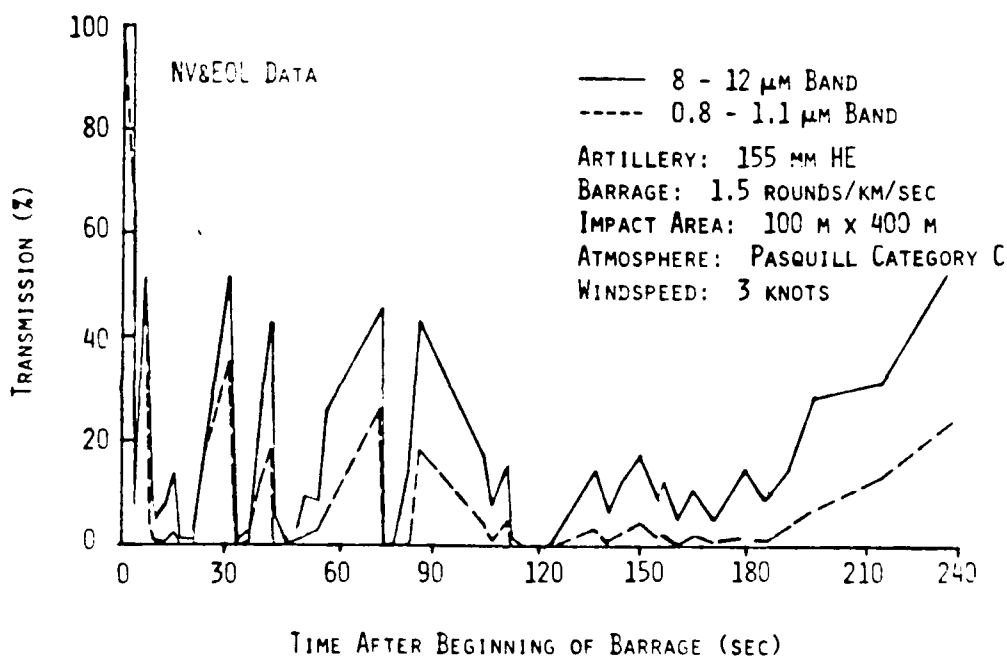
Figure 2. Transmission in the 8-12 μm and 0.8-1.1 μm Band During a 155 mm HE Barrage at Grafenwohr, Germany. In this situation, transmission in excess of 20 - 40% occurred at numerous times during the barrage. (Data from the Graf II test conducted by the Night Vision & Electro-Optics Laboratory, Ft. Belvoir, VA, November 1978.)

12

Despite this reduced barrage intensity and increased aerosol dispersion, the
TAPATS test still had an order of magnitude less transmission. The reason
for the enhanced transmission in Fig. 2 vis-à-vis Fig. 1 will become manifest
upon the following discussion of the two basic steps in the determination of
the dust source term.

2.1.1 Mass of Airborne Ejecta

There is an extensive background (see for example Ref. 2) of theoretical
analysis and empirical correlations for cratering mechanics and phenomenology.
Dimensional analysis readily shows[3] that the governing parameters are the
density of the soil, its elastic and plastic moduli, the gravity acceleration,
and the energy coupled into the ground. In fact, the crater volume can be
calculated from numerical integrations of the conservation equations for mass,
momentum, and energy together with the equation of state,[4] to obtain results
in reasonable agreement with observations. However, the execution of these
calculations is quite burdensome and the number of available examples is limited.
Therefore, one cannot extract the systematic dependence of the crater volume on
elastic and plastic properties of various soil types. The difficulty has been
remedied in practice by the use of empirical correlations of the very extensive
crater volume data basis.[5] In these correlations, the scaled crater radius
$\overline{r}_c$ and depth $\overline{d}_c$ are predicted as a function of a scaled charge depth λ_c and
qualitative soil characterizations (e.g., dry and moist cohesive). Analytical
fits to the dependence of crater dimensions $\overline{r}_c$ and $\overline{d}_c$ as a function of λ_c and
soil category have been presented in Ref. 6 and are included in the DIRTRAN-I
code. Specifically, for bare-charge explosions

$$\overline{r}_c = a_0 + a_1 \lambda_c + a_2 \lambda_c^2 + a_3 \lambda_c^3$$

$$\overline{d}_c = b_0 + b_1 \lambda_c + b_2 \lambda_c^2 + b_3 \lambda_c^3 + b_4 \lambda_c^4$$

13

where

$$\bar{r}_c = (r_c/W^{1/3}) = \text{scaled crater radius in units of } (m/kg^{1/3})$$

$$\bar{d}_c = (d_c/W^{0.3}) = \text{scaled crater depth in } (m/kg^{0.3})$$

$$\lambda_c = (d_b/W^{1/3}) = \text{scaled explosion depth in } (m/kg^{1/3})$$

$$W = \text{energy release of charge in equivalent kilograms of TNT}$$

These coefficients, a_0, ..., a_3 and b_0, ..., b_4 are listed in Tables 2-1 and 2-2. Their average values for the various soil categories recognized in Ref. 5 are shown in Figs. 3 and 4. The usefulness of these curve fits is apparent from the mean crater volumes observed in the DIRT I series (Fig. 5).[7] They correspond to a soil intermediate between "dry sandy soil" and "dry-to-moist sand." Since this site is characterized as "brown silty sand" with an average of 7% moisture,[8] the qualitative description is reasonable. Similarly, for the Graf II-Winter test, the mean crater volume corresponds to a "wet sand" type soil, which appears consistent with a description of " loamy sand/sandy loam" with an average moisture content of 20%.[9] The coefficients appropriate to these soils are incorporated in the DIRTRAN-I code as descriptive of "Desert" and "European" conditions, respectively.

The tabulated coefficients must be unique functions of the elastic/plastic parameters indicated by dimensional analysis. Thus, it would seem highly desirable to replace the qualitative characterization of soils with a statement of mean values of elastic/plastic parameters appropriate to each category. Static laboratory measurements of an adequate number of soil samples for each category can yield the values of such parameters. Thereafter, the determination of crater volume would be uniquely related to the measurement of specific elastic/plastic properties. It should be noted that crater measurements at a single test site (e.g., see Refs. 7-9 for the DIRT I and Graf II-Winter tests) show scatter in crater volume data of typically ±20% (cf. Fig. 5). It would be interesting to correlate this scatter with that exhibited by corresponding measurements of the elastic/plastic moduli.

Table 2-1. Coefficients for Average Scaled Crater Radius

Coefficient / Category	a_0	a_1	a_2	a_3
I, II	0.271	-0 684	0.390	0.886
III	0.386	-0.849	0.367	0.993
IV	0.503	-0.954	0.450	1.19
V, VI	0.629	-1.08	0.264	1.12
VII	0.806	-1.28	-0.178	0.852

Table 2-2. Coefficients for Average Scaled Crater Depth

Coefficient / Category	b_0	b_1	b_2	b_3	b_4
I	0.113	-0.477	0.270	1.84	1.05
II	0.134	-0.571	0.343	2.24	1.32
III, V	0.189	-0.840	0.447	3.30	2.10
IV	0.251	-1.17	0.494	4.72	3.34
VI	0.331	-1.49	0.579	4.92	3.13
VII	0.449	-1.82	0.322	4.11	2.02

Category	Description
I	Rock
II	Dry Cohesive Soils (Lightly Cemented)
III	Dry Sandy Soils
IV	Dry-to-Moist Sand and Frozen Ground
V	Soft Rock
VI	Wet Sand, Moist Cohesive Soils, and Ice
VII	Wet Cohesive Soils (Not Saturated) and Snow

15
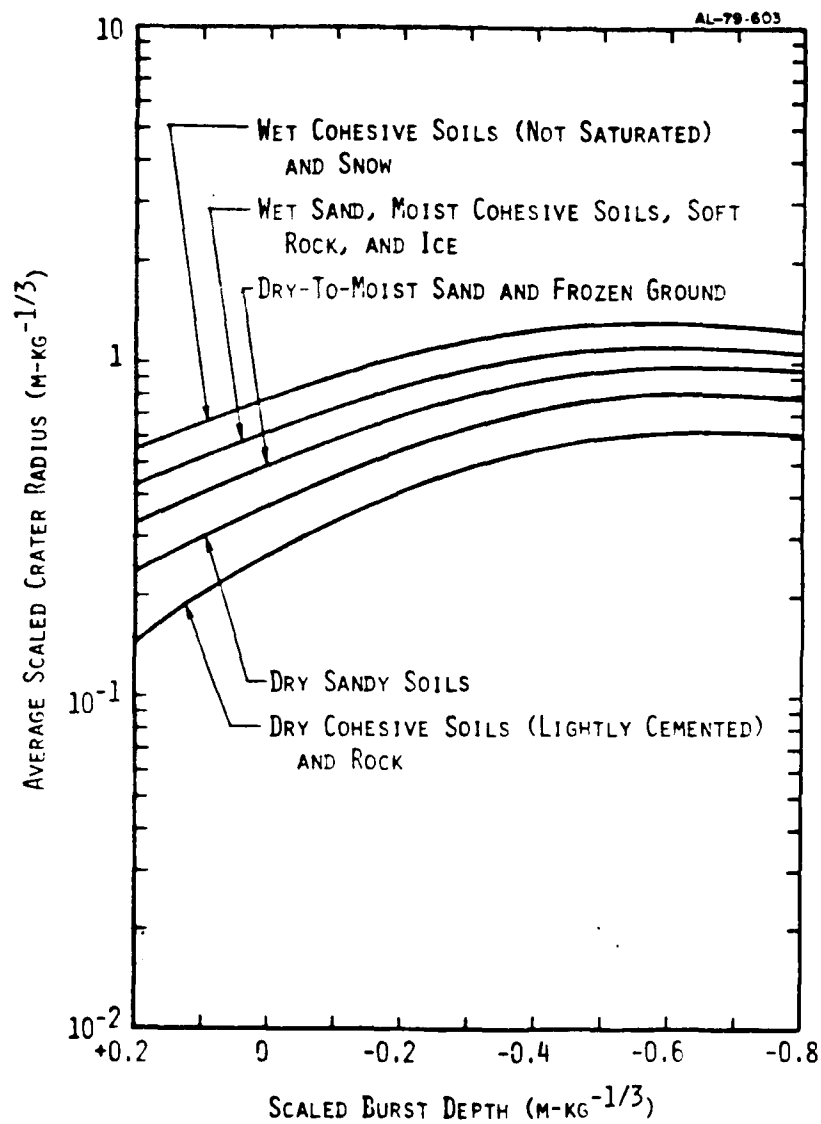
Figure 3. Average Scaled Crater Radius Versus Scaled Burst Depth for Different Soil Characterizations (Ref. 5) Using Coefficients From Tables I and II (Ref. 6)
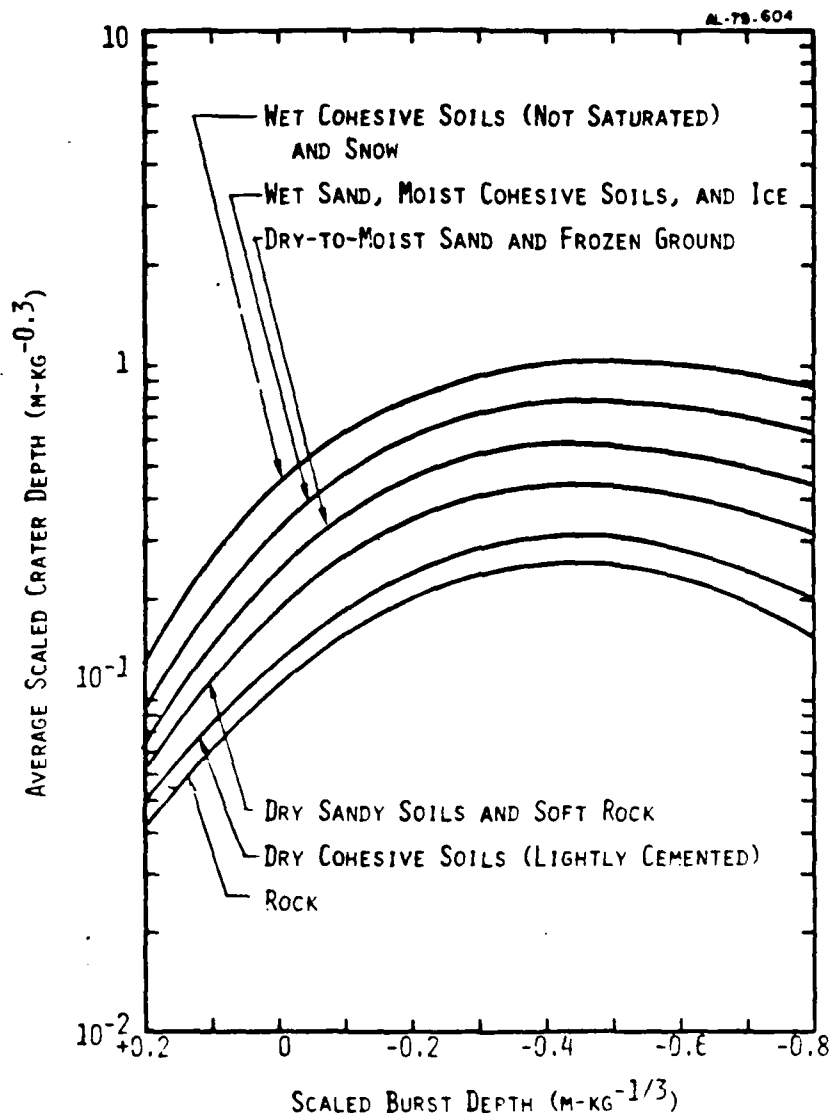
Figure 4.   Average Scaled Crater Depth Versus Scaled Burst Depth
for Different Soil Characterizations (Ref. 5) Using
Coefficients From Tables I and II (Ref. 6)

17
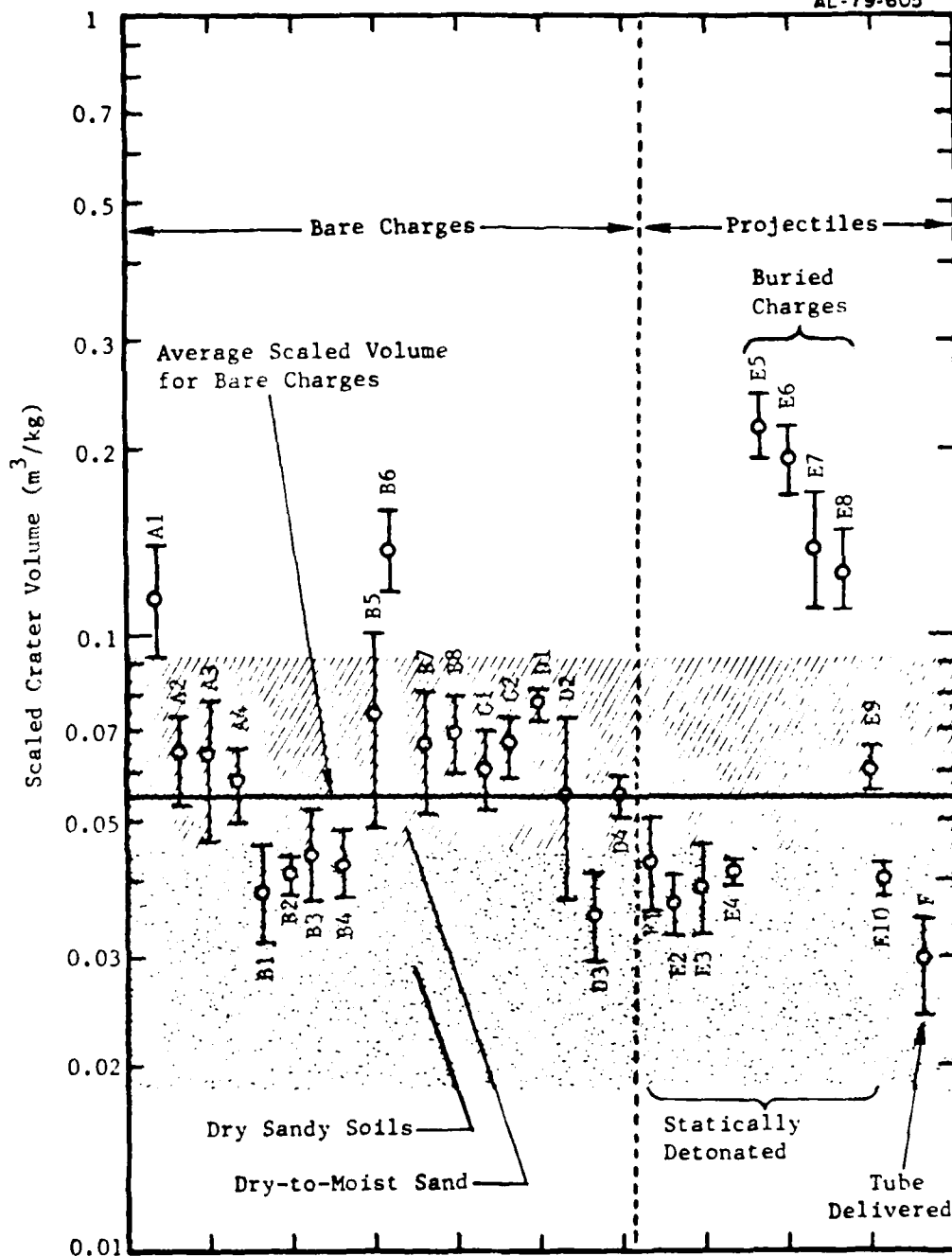
Figure 5. Scaled Crater Volume (Product of Crater Radius Squared and Crater Depth Divided by Explosive Charge Weight -- $r_c^2 d_c/W$) With Standard Deviation of Measurements for the 29 Explosion Events in the DIRT I Test (Ref. 7). The bare-charge events (all surface detonations) resulted in scaled crater volumes corresponding to the dry/dry-to-moist sandy soil categories of Ref. 5. Tube-delivered projectiles and projectiles statically detonated on the surface resulted in scaled crater volumes which were, respectively, 40% and 20% smaller than those resulting from bare charges. Buried projectiles produced larger scaled crater volumes.

18

Our DIRTRAN studies show that, at nominally fixed soil characteristics, a vegetative cover produces an incremental deposition of crater material at the lip. This effect, visibly evident in Fig. 6, can account for the different transmission characteristics exhibited in Figs. 1 and 2. Vegetative cover effectively reduces the (elliptical) crater volume (Fig. 7) according to the equation

$$V_c = \frac{2}{3} \pi r_c^2 d_c \left\{ 1 - \frac{3}{2} \frac{d_s}{d_c} \left[1 - \frac{1}{3} \left(\frac{d_s}{d_c} \right)^2 \right] \right\}$$

where

V_c = crater volume which contains only soil (i.e., no sod)

r_c, d_c = crater radius, depth as determined in accord with Refs. 5 and 6

d_s = sod depth

An additional correction to crater volume arises in connection with the explosion of bare charges vis-à-vis casing - enclosed charges (e.g., artillery shells). For fixed weights of explosive and terrains, the crater size directly depends on the fraction of released energy which is coupled into the ground. Not only does this fraction vary with the explosion depth as noted above, but also with either the presence or the absence of a charge casing. For 155 mm artillery projectiles carrying 6.8 kg of TNT, the crater volume yield (Fig. 5) is approximately 60% of that of an equal weight bare charge (Ref. 7). This evidence is rationalized upon inspection of the energy balance for an explosion.

First, let us consider the influence of tube launch. For 155 mm projectiles, the kinetic energy associated with a 400 m/s impact velocity is 14% of the explosion energy; its contribution to increased crater volume is thus hardly detectable within the accuracy of the crater volume measurements (± 20%). Second, let us consider the effect of casing (Fig. 8). Upon explosion, the energy is partitioned between air, soil, and (in the case of the projectile) shell fragments. For a bare charge, the partitioning is largely determined by the compressibility (elastic modulus) of the air and soil media

19

Figure 6. Graf II Test 155 mm HE Artillery Round Craters. Depth of
vegetative sod cover is approximately 25 cm, comprising a
large portion of the crater volume.

FT. KNOX, KY.
TEST RANGE
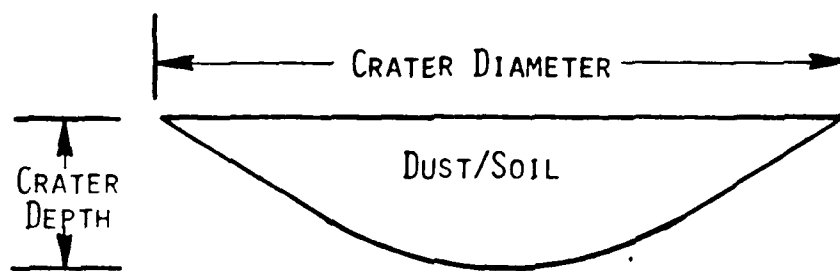
GRAFENWOHR, GERMANY
TEST RANGE
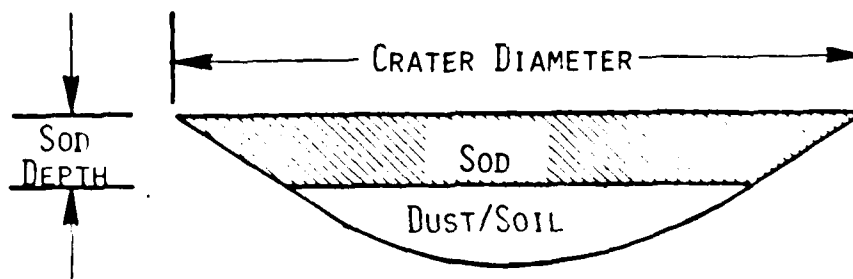
Figure 7. Effect of Sod (Vegetative Cover) on Crater Volume. The sod
depth is drawn here roughly to scale for the Graf 11 test
for the 155 mm HE artillery round craters. The volume of
soil (which is available for production of entrained dust)
is seen to be only a small fraction of the total crater
volume.

Bare Charge (No Casing)

(a) Explosive
     Energy

Air (90-95%)

Air (100%)

Soil Kinetic Energy (5-10%)

Soil Deformation (<1%)

Projectile

Fragments
Moving Up (40%)

Fragment
Kinetic
Energy(40%)

(b) Explosive
     Energy

Fragments
Moving Down 40%

Air (36-38%)

Soil K.E.(2-4%)

Air (60%)

Air (18-19%)

Soil Kinetic Energy (1-2%)

Air (20%)

Soil Deformation (<1%)
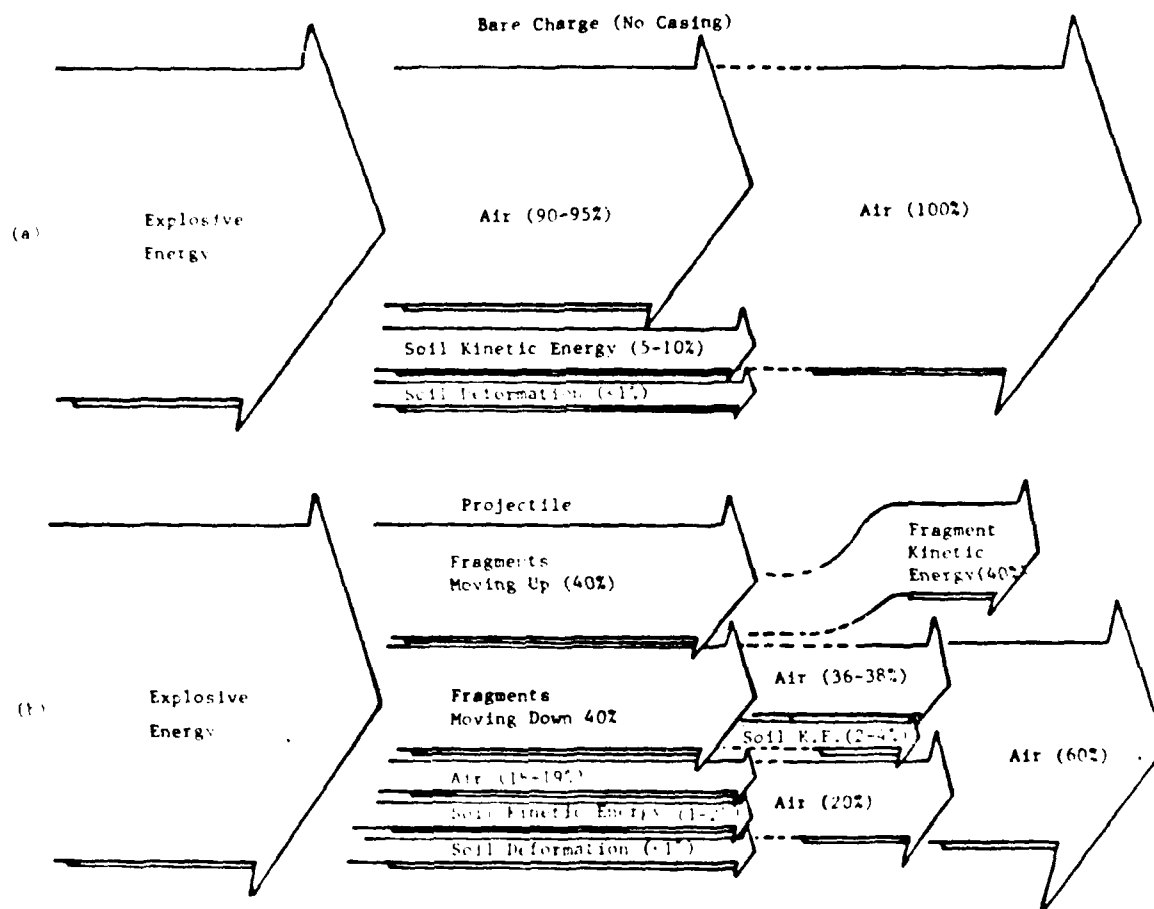
Figure 8. Energy Budget for Surface Explosions.
           (Identical Charge Size) (a) Bare Charge
           (No Casing); (b) Projectile

22

and by the requirement of continuity at the soil/air interface (often referred to as impedance matching) subsequent to the passage of the explosion-produced shock waves in the two media. Detailed cratering calculations[4] show that typically 5 - 10% of the energy is coupled into the soil.* Therefore, for a bare charge exploded at the surface, 90-95% of the explosive energy is immediately coupled into the air.** Ultimately, the remaining 5-10%, initially coupled into kinetic energy of the crater ejecta, is also transferred to the air by aerodynamic arrest of the particles, as depicted in Fig. 8a.

The explosion of a projectile leads to a different initial partitioning of energy (Fig 8b); the following arguments indicate that an appropriate estimate for the explosive energy transferred to shell fragment kinetic energy is 80% with 20% directly transferred to the air thermal energy. Shell fragments generated by the upper portion of the exploding shell escape ballistically from the domain of influence of the explosion. By contrast, the shell fragments generated by the lower half readily impact the ground and thereupon transfer their kinetic energy partly to the air and partly to the soil. These transfers are roughly in the same proportion found in a bare charge explosion because of the impedance matching requirement referred to above and discussed in Ref. 4. As a result, the energy coupled to the soil is approximately 40% less than the equivalent bare charge explosion; consequently, the crater is also reduced by 40%, consistent with the results reported in Ref. 7. The energy ultimately coupled into the air is also reduced by about 40%,** again consistent with the data, e.g., Fig. 9 where the development of buoyant clouds produced by equal weight bare and enclosed (projectile) charges are shown. Clearly, the energy loss due to shell fragments results in smaller buoyancy available for cloud rise.

---

* The same estimate can be obtained upon calculation of the kinetic energy of the ejecta. For example, a 1 kg charge of TNT (4.7×10^6 J energy) exploded on the surface of dry/dry-to-moist sand (e.g., White Sands DIRT I soil) produces a 0.11 m^3 crater. Using an estimated average initial ejecta velocity of 60 m/sec (Ref. 10) and a specific gravity of 1.6, the total kinetic energy of the ejecta is then 3.2×10^5 joules, i.e., only 0.067 of the energy released by the explosion.

** These estimates lead to dual predictions, namely, crater size as well as buoyant cloud size, which, as shown below, compare favorably with measured data.
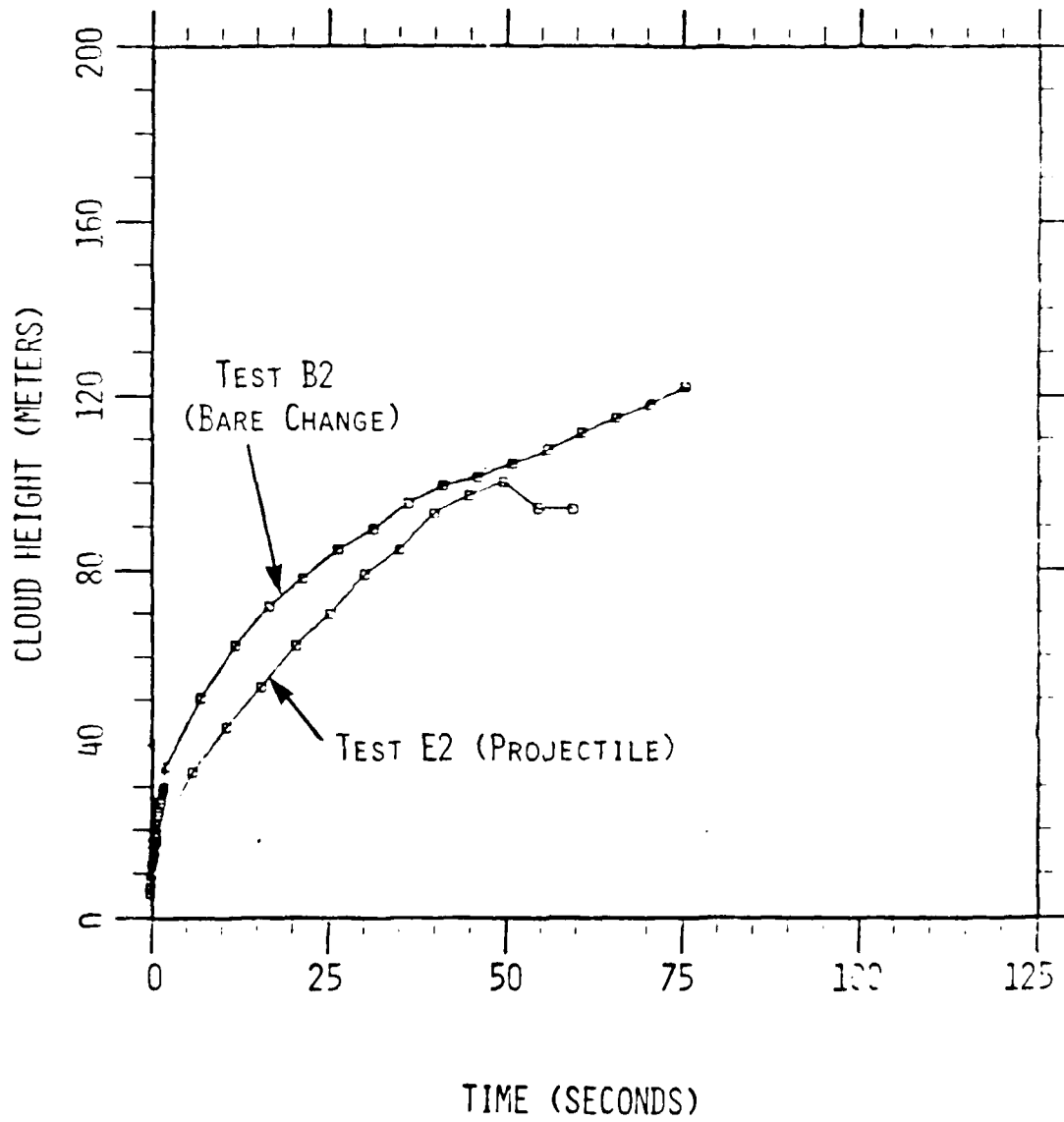
Figure 9. Comparison of Buoyant-Rise Cloud Height Data for 6.8 kg TNT Charges With and Without Projectile Metal Casing

Another consideration concerning the dust source term relates to the fact
that only a fraction of the crater material is injected into the atmosphere,
the balance, having a small ejection velocity, is deposited on the crater lip.
As mentioned above, the explosive energy coupled to the ground is typically
fixed to the range 5-10%, i.e., it varies at best by a factor of 2. How-
ever, the crater volume for different soil types can vary by a factor of
40 for surface explosions, as evidenced by Figs. 3 and 4. Thus, by conserva-
tion of energy for a given charge, the kinetic energy per unit mass of the
ejecta associated with the largest craters must be substantively smaller (by
a factor of the order of 20-40) than the kinetic energy per unit mass of the
ejecta from the smallest craters. Correspondingly, the initial velocities of
the large-crater ejecta must be smaller by a factor of the order of 4-6, and
the fraction of the ejecta deposited around the crater rim must thus be larger
than for small crater cases. For example, for explosions in granite as shown
in Fig. 10 (Ref. 10), 60% of the crater ejecta is deposited on the crater rim
and 40% becomes airborne. From the kinetic energy considerations stated
above, and under the assumption of identical impedance matching, the airborne
material yielded by an explosion in wet cohesive soils could be reduced by a
factor of 4-6, i.e., only 7-10% of the crater mass becomes airborne while
90-93% is deposited on the rim. These percentages only represent crude
estimates. However, they suggest almost an order of magnitude impact on the
amount of material becoming airborne. Thus, either systematic cratering cal-
culations or systematic experiments focused on the determination of crater
rim ejecta are essential to the realistic determination of soil entrainment
in the dust clouds.

2.1.2 Comminution/Agglomeration of Ejecta

Even if the factors listed above are taken into account and the mass of
dust injected into the atmosphere determined accordingly, the aerosol is not
characterized either aerodynamically or optically. Thus, part two of the
present problem is posed, namely: the estimation of the dust particle size

25
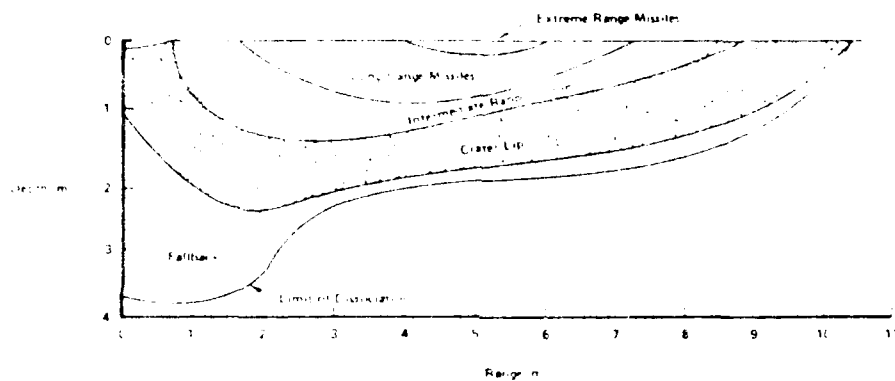
Figure 10. Zones of origin of crater ejecta for a 100-ton TNT
explosion in granite (Ref. 10). The apparent crater
volume is equal to the volume of the particle "missiles"
which travel ballistically and the material deposited
on the crater lip. For this test, the crater lip
material comprised 60% of the apparent crater volume.

distribution function. On aerodynamic grounds, this is important because all particles having diameter $D \gtrsim 100$ µm escape ballistically (cf. Appendix A) and thus never partake in the formation and subsequent buoyancy/wind-controlled diffusion of the obscuring cloud. On optical grounds, the determination of the distribution function controls the transmission along any line of sight through the cloud even though the total mass and dielectric properties of the intervening aerosol may be known. Unfortunately, the "process of comminution of crater material has not been described either theoretically or experimentally"[10]

Up to the present time, dry-soil sieve analyses have been used as a measure of the distribution function to be encountered in explosion-generated clouds. However, prima facie evidence suggests that this may be a poor assumption. Specifically, photographs (Fig. 11) of the ejecta deposited on the crater rim indicate the presence of an appreciable amount of large chunks of soil (≈ 5-8 cm diameter). This is not reflected in the sieve analyses, such as shown in Figs. 12 and 13 (which represent extreme values in large particles mass fraction indicated by the sieve analysis). In either case, no more than 1% (at most) of the mass is associated with particles having diameter $L \gtrsim 1$ cm, in contradiction with the photographic data. The studies of optical transsion data reported in Section V also suggest a marked depletion of fine particles relative to the amount indicated by sieve analysis. In fact, the studies indicate that particle agglomeration constitutes the largest uncertainty factor in the determination of the optical effects of explosion-generated dust clouds. The issue warrants immediate attention. Dynamic soil tests which involve the failure of material subjected to strong wave pulses and which can provide systematic measurements of the attendant soil/sod fragment distribution function are recommended as indispensable prerequisites to the systematic determination of the airborne dust source term.

2.2 Initial Dust Clouds

Inspection of data, such as in Fig. 14, readily reveals that the initial dust cloud is partitioned into two parts, one buoyant, one nonbuoyant. The
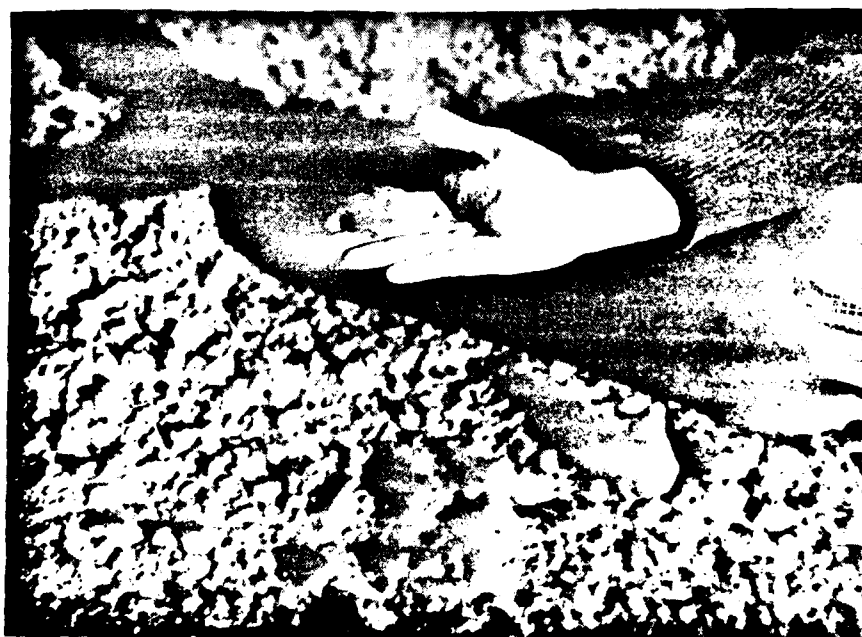
Figure 11. Effect of Dynamic (Explosive) Loading on Comminution/
            Agglomeration of Soil in the DIRT I Test Series. Note
            presence of large ($\approx$ 5-8 cm diameter) crater ejecta.

Figure 12. Particle Size Distribution Obtained by Dry-Soil Sieve
Analysis for DIRT I Test Site. Note maximum particle
size indicated is 0.5 cm (Ref. 8).

29
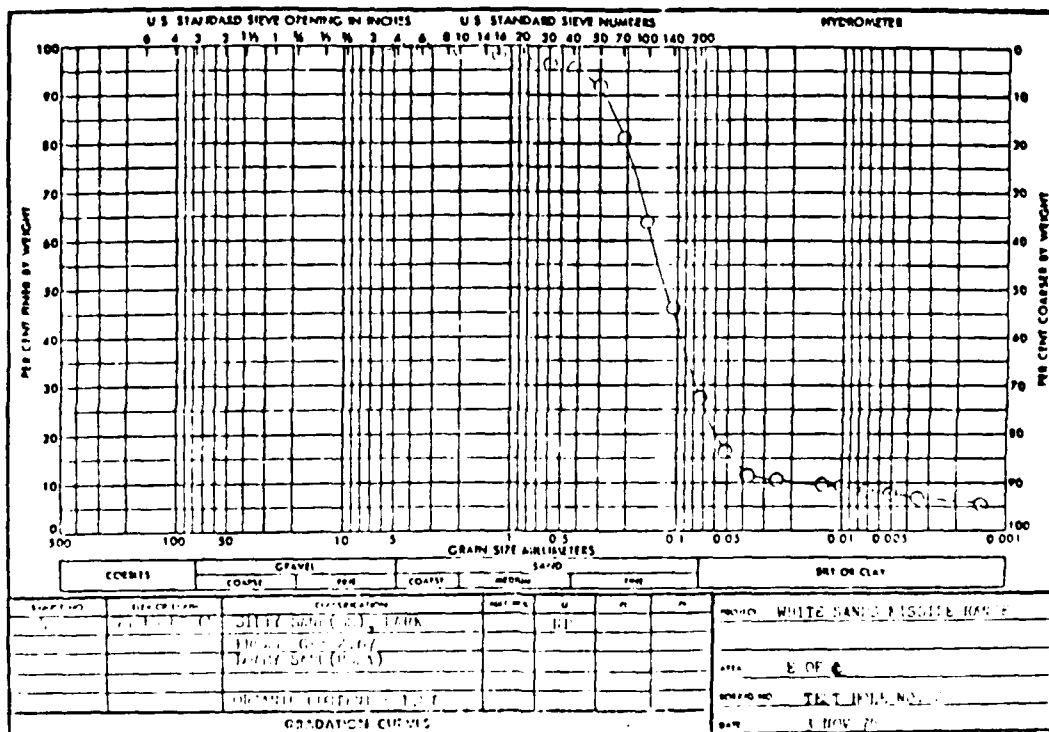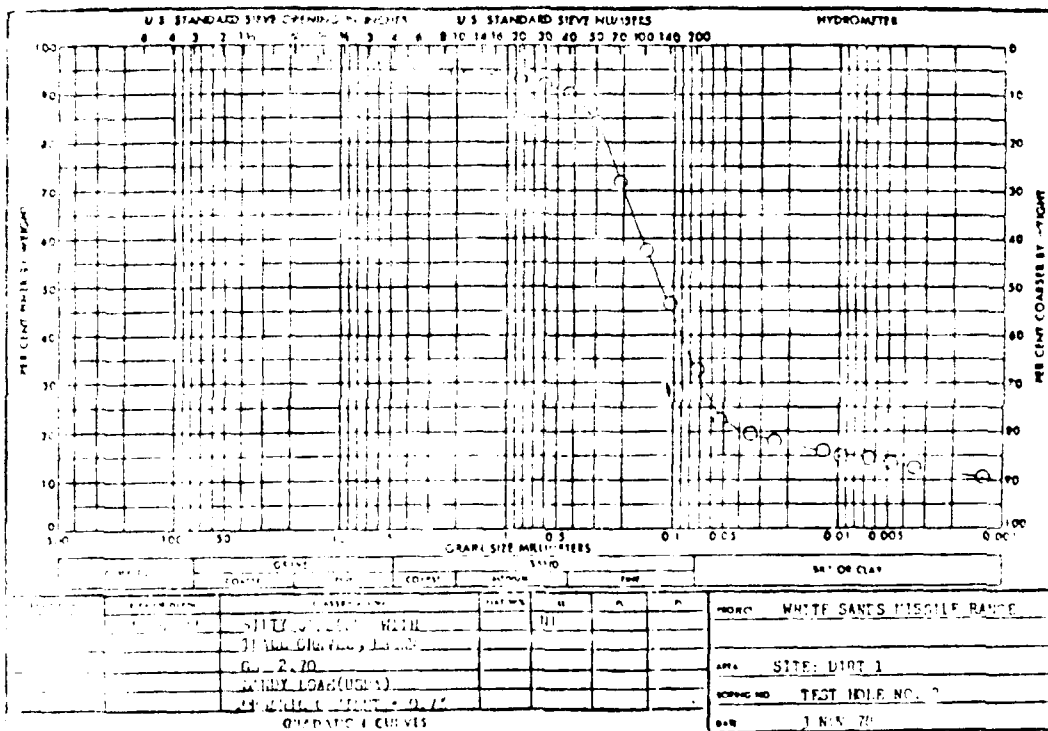
Figure 13. Particle Size Distribution Obtained by Dry-Soil Sieve
Analysis for DIRT I Test Site. For this sample,
maximum particle size indicated is 1.8 cm (Ref. 8).

Dust Particles Entrained
in Buoyantly Rising
Hot Gases

Dust Particles Entrained
in Nonbuoyant
Dust Skirt

Figure 14(a). Example of Entrainment Partitioning of Explosion-
Produced Soil Ejecta Inside and Outside of Hot
Gases From Explosion (Source: DIRT I Test Series)
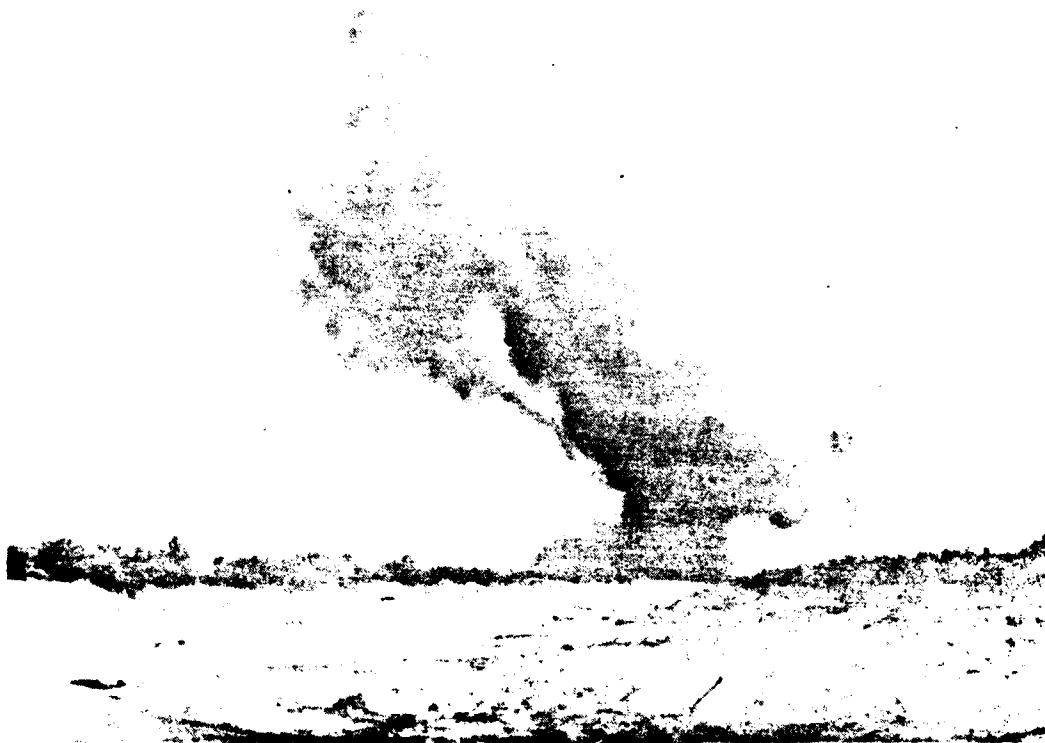
Figure 14(b). Example of Buoyant Rise Effects on the Dispersion of
               Explosion-Produced Dust Clouds. The effect of a mild
               wind which causes the rising cloud to follow a slanted
               path is evident. Noticeable too is the persistence of
               the nonbuoyant "dust skirt" which is near the ground
               and which has significant effects on ground-based
               EO Systems (Source: DIRT I Test Series).

geometry of these clouds can in principle be predicted by coupled simultaneous time-dependent, two-dimensional calculations of the soil cratering process and the aerodynamic blast propagation process on time scales of the order of 10^{-2} sec for typical artillery explosions. Such calculations are not available because the requirement for them has not been evidenced heretofore. One must, at present, resort to data analysis and correlations guided by basic scaling criteria with length scales proportional to the cube root of the explosion energy release.

2.2.1 Buoyant Dust Cloud

Whereas the explosion energy balance discussed in Section 2.1 above indicates the amount of energy coupled into the air, the attendant size of the buoyant dust clouds can be estimated on the basis of well-established correlations of hydrodynamic blast calculations in uniform media of infinite extent (Ref. 12). Thus, the initial buoyant cloud radius is given by

$$R_o = 2.0 \, W_{eff}^{1/3} \, (\rho_o/\rho)^{1/3}$$

where R_o is in units of meters; W_{eff} is the effective energy coupled to the air in units of kilograms of TNT; ρ_o and ρ are the densities of air at sea level and at the blast site, respectively. The excess temperature ΔT of the cloud over ambient air follows from conservation of energy;

$$\frac{\Delta T}{T_a} = \frac{E_{eff}}{V_o \rho_a c_p T_a} \left(1 - \frac{E_{eff}}{V_o \rho_a c_p T_a} \right)^{-1} \approx 0.57$$

where

E_{eff} = energy coupled into air = kW_{eff}

k = energy equivalence of TNT = 1.1×10^3 kcal/kg (Ref. 13)

V_o = initial cloud volume = $\frac{4}{3} \pi R_o^3$

ρ_a = ambient air density = 1.25 kg/m^3

33

c_p = heat capacity of air = 0.24 kcal/kg

T = ambient temperature (assumed $\cong 288^\circ$K)

... the initial dust cloud temperature T is 1.57 T_a (i.e., T = 452°K for T_a = 288°K).

The calculations presented in Ref. 12, however, do not predict the loca- ... the initial buoyant cloud at the end of the aerodynamic transient, ... as the cloud ... with the cloud achieves pressure/velocity equilibra- ... with the ambient atmosphere ... mentioned above, ... made with the initial cloud size R_o. Inspection of the DIPl I cloud height data (Ref. 14) for bare charges exploded on the surface demonstrates that the height of the cloud centroid ($z = h-R_o$, where h is the height of the top of the ... scales with R_o and reaches the value $5R_o$ at the end of the aerodynamic transient time $t_d = t/R_o \cong 0.15\ R_o$ (for t_d in seconds, R_o in meters). If the charge is not exploded on the surface, the asymptotic value of the centroid height changes. However, limited data prevent a completely satisfactory correlation. For example, it appears that for explosions of tube-delivered artillery projectiles, this centroid displacement is reduced to zero (i.e., $z = R_o$).

Little direct information is available with regard to initial mass load- ing in the buoyant cloud. Because typical optical transmission line-of-... are limited to heights less than 5m, they intersect the buoyant cloud ... small fraction of a second (less than 0.1 second), at which time ... are opaque for the wavelengths and charge sizes employed in the DIPl I ... Graf II series. Hence, only lower bounds for the mass loading can be deter- mined from these data. Observation of cloud dissipation at late times (cf. Section V) indicate that perhaps 50% of the small size comminuted agglomerated ejecta are contained in the buoyant cloud. This only represents a rough estimate which must be improved in the future. Reduced scale experiments with smaller charge sizes could greatly resolve this issue. These experiments should be executed in the broader context of answering the question of initial airborne ejecta mass, comminution/agglomeration, and velocity.

34

2.2.2 Nonbuoyant Dust Skirt

The existence of nonbuoyant cloud portions is forcefully demonstrated not only by photographic data (as shown in Fig. 14) but also by the long duration of optical degradation along lines of sight near the ground. The trends in the optical data discussed in Section V show that these "dust skirts" diffuse under the action of the wind. The initial dimensions of the skirt must again scale together with the buoyant-cloud characteristic dimension R_o. Inspection of typical cloud contour maps such as shown in Figs. 15 and 16 (Ref. 15) suggest that the skirt of an individual explosion can be approximated by upright cylinders of radius $2R_o$ and height $2R_o$.[*]

---

[*]The data in Figs. 15 and 16 are for an array of three simultaneous explosions oriented perpendicular to the line-of-sight and separated by a distance d = 15m. Thus, the apparent initial cloud width for three charges is $2(d + 2R_o)$. Accordingly, one predicts for Test B-2 and B-7 (charge sizes 6.8 kg and 55 kg TNT, respectively) apparent widths of 45m and 60m which compare reasonably well with the observed values of 44m and 54m.

EVENT #B2   T+ 0.5 SEC.

        DUST   CENTROID(REF. IGNITION PT.)   ELLIPSE
HEIGHT= 17. METERS   HEIGHT= 11. METERS   MAJOR AXIS= 44.7 METERS
WIDTH= 44. METERS   OFFSET= -3. METERS   MINOR AXIS= 16.9 METERS
AREA= 481.3 SQ METERS   INCLINATION= 3 ODEGREES

HEIGHT ABOVE IGNITION POINT   20. METERS

CONTOUR GRAYLEVELS   140 160 180 200 220 240
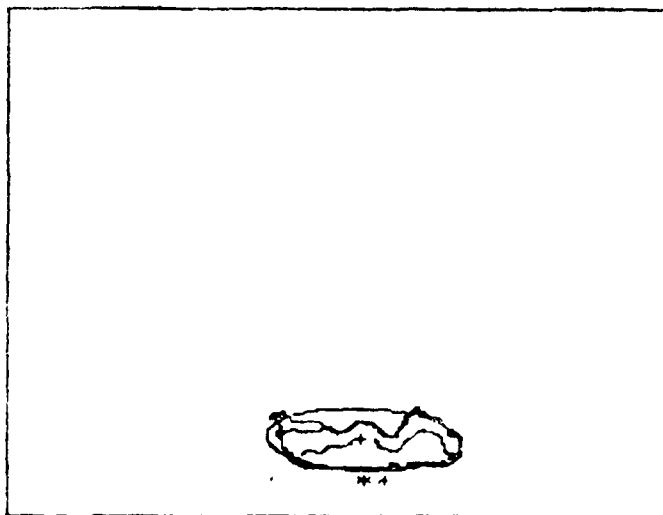
ATMOSPHERIC SCIENCES LAB
WHITE SANDS MISSILE RANGE   N M

Figure 15.   Computer Generated Contour Plots of Dust Clouds Formed in
             Event B-2 of the DIRT-I Test 0.5 sec After Detonation.
             Note presence of three overlapping clouds due to the
             three 6.8 kg charges. As reported, the width is 44 meters.
             The separation between charges is 15m. Each individual
             cloud is approximately 14m in diameter (Ref. 15).

TRIAL #B7   T+ 0.5 SEC.

DUST   CENTROID(REF. IGNITION PT.)   ELLIPSE
HEIGHT= 30. METERS   HEIGHT= 13. METERS   MAJOR AXIS= 49.1 METERS
WIDTH= 54. METERS   OFFSET= -5. METERS   MINOR AXIS= 27.6 METERS
AREA= 833.8 SQ METERS   INCLINATION= -7.1DEGREES

HEIGHT ABOVE IGNITION POINT   29. METERS

CONTOUR GRAYLEVELS: 135 150 160 170 180 190
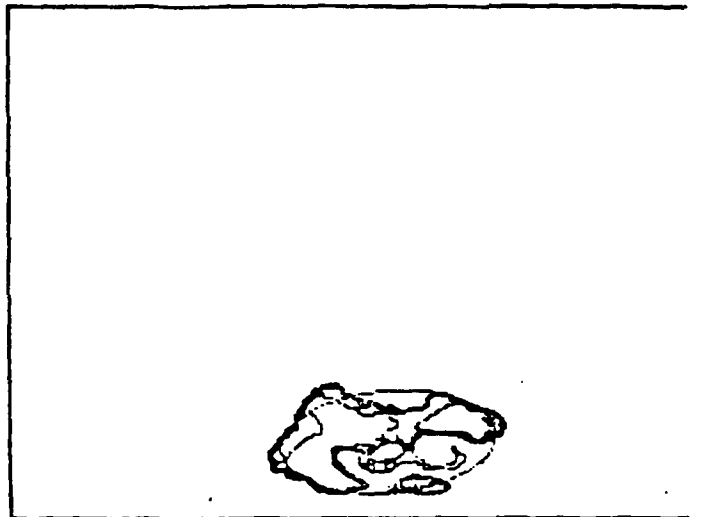
ATMOSPHERIC SCIENCES LAB
WHITE SANDS MISSILE RANGE. N M

Figure 16.   Computer Generated Contour Plots of Dust Clouds Formed in
             Event B-7 of the DIRT-I Test 0.5 sec After Detonation.
             Note presence of three overlapping clouds due to the
             three 55 kg charges. As reported, the width is 54 meters.
             The separation between charges is 15m. Each individual
             cloud is approximately 24m in diameter (Ref. 15).

37

3. ATMOSPHERIC DIFFUSION

The buoyant cloud evolves at first like a thermal. When the rate of diffusion due to buoyant rise becomes equal to that associated with the turbulent wind field, the buoyant cloud development becomes controlled by the latter. The dust skirt evolution is controlled throughout by wind-generated turbulence. Qualitative dust cloud patterns as calculated by the DIRTRAN model are exhibited in Figs. 17, 18, and 19 (Ref. 11). Details of the model statement are described below.

3.1 Buoyant Cloud Rise and Diffusion

This process is described by the model of Ref. 16 for a thermal. With the notations b, A, and V for the cloud radius, surface area, and volume respectively; u for the rise velocity (z-direction), assumed uniform throughout the cloud; v for the horizontal cloud velocity, assumed equal to the local wind velocity; $\Delta\Theta$ for the cloud excess potential temperature relative to local potential temperature Θ_a; the conservation equations of mass, momentum, and energy take the form

$$\frac{db}{dt} = \alpha u \tag{3-1}$$

$$\frac{du}{dt} = -\frac{\Delta\Theta}{\Theta_a}\left(-g + \frac{A}{V}\alpha u^2\right) \tag{3-2}$$

$$\frac{d(\Delta\Theta)}{dt} = -u\frac{d\Theta_a}{dz} - \frac{A}{V}u\alpha\Delta\Theta\left(1 + \frac{\Delta\Theta}{\Theta_a}\right) \tag{3-3}$$

where α is an empirical entrainment coefficient equal to 0.25 according to numerous experiments (Ref. 17) and g is the gravitational acceleration. Equations (3-1) to (3-3) are integrated subject to initial conditions at $t = 0$

DIRTRAN CALCULATION
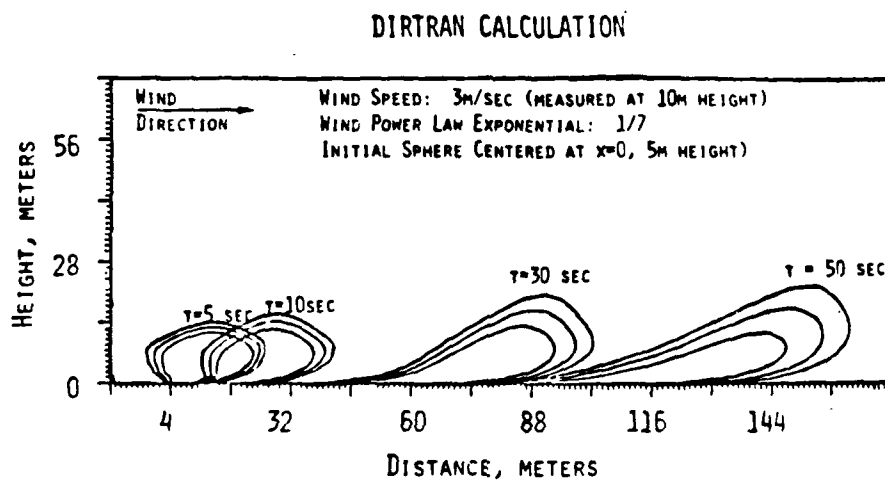
Figure 17. Wind controlled diffusion of nonbuoyant dust skirt with no gravitational settling. Time sequence of contours of line-of-sight integrals of dust concentration (i.e., $C\ell$ values) were computed by the DIRTRAN model. The three contours represent, respectively, 0.1, 0.05, and 0.025 fractions of the initial average $C\ell$. Note the effect of wind shear. (Ref. 11)

DIRTRAN CALCULATION
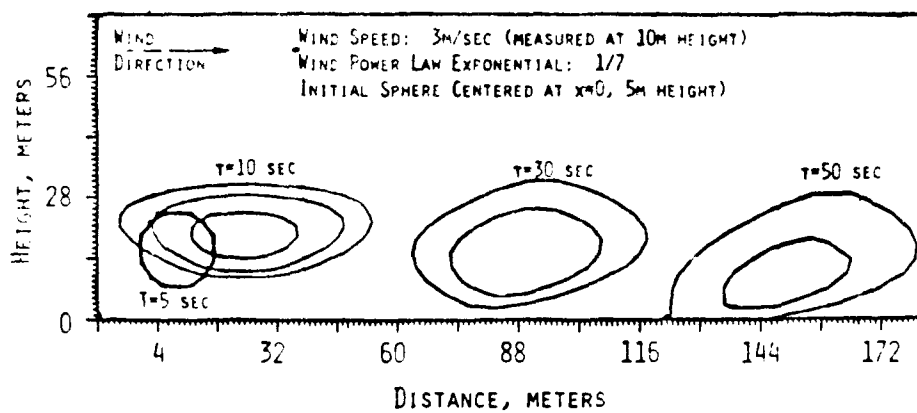
Figure 18. Sequential buoyancy and wind-controlled diffusion of
a dust cloud in a neutrally stratified atmosphere
with gravitational settling (50 μm diameter particles).
Contours are same as for Fig. 17 with no 0.1 contour
after 30 seconds. (Ref. 11)

DIRTRAN CALCULATION

WIND
DIRECTION → WIND SPEED: 3M/SEC (MEASURED AT 10M HEIGHT)
WIND POWER LAW EXPONENTIAL: 1/7
INITIAL SPHERE CENTERED AT X=0, 5M HEIGHT)

HEIGHT, METERS
56
28
0

T=10 SEC   T=30 SEC   T=50 SEC

4   32   60   88   116   144   172

DISTANCE, METERS
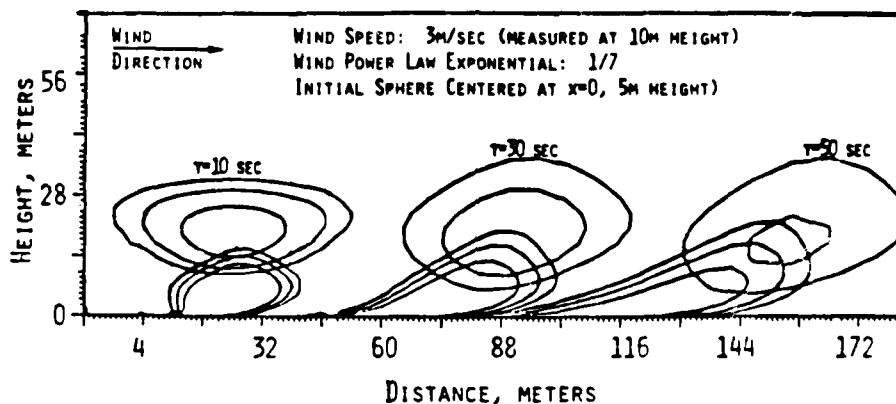
Figure 19. Superposition of Wind and Buoyancy Controlled Diffusion of Small
Particles. The time-sequence of contours of line-of-sight
integrals of dust concentration (i.e., Cℓ values) were computed
by the DIRTRAN model for 0.1, 0.05, and 0.025 fractions of the
initial average line-of-sight integral of particle concentra-
tion. Note the strong wind shear effect with altitude, an
important phenomenon for near-ground line-of-sight obscuration
effects. (Ref. 11)

41

$$b(0) = R_o$$

$$u(0) = 1.3 R_o^{1/2} \quad (u \text{ in m/sec, } R_o \text{ in m})^*$$

$$\frac{\Delta\Theta(0)}{\Theta_a} = 0.57$$

$$z(0) = \begin{cases} 5R_o & \text{for bare charges detonated at the surface} \\ R_o & \text{for tube-delivered 155 mm artillery shells with} \\ & \text{fuzing as used in the DIRT I test} \end{cases}$$

Upon integration of Eqs. (3-1) to (3-3), the height $h(t)$ at the top of the cloud, the centroid height $z(t)$, and the cloud width $d(t)$ are calculated as

$$z(t) = z(0) + \int_0^t u \, dt \qquad (3\text{-}4)$$

$$h(t) = z(t) + b(t) \qquad (3\text{-}5)$$

$$d(t) = 2\, b(t) \qquad (3\text{-}6)$$

The vertical distributions of potential temperature $\Theta_a(z)$ and wind velocity $v(z)$ are described according to atmospheric stability condition as detailed in Appendix B.

Predictions of this model are compared with data in Section 5.

3.2 Wind-Dominated Cloud Diffusion

The process of wind-controlled diffusion, taking into account the actual vertically sheared wind profile, is described by the differential equation of diffusion. The action of turbulence is represented on a long-time average basis by the gradient transfer relation. The diffusivities in the three

---

*This initial velocity can be extracted from the point source solution (Ref.16) and is found to agree with the data for cloud rise velocity from the DIRT I test.

42

coordinate directions are prescribed consistent with the stability character-
istics of the atmospheric boundary layer. Aerosols are subjected to gravi-
tational settling (at their size-dependent terminal velocity) in addition to
diffusion.

The initial cloud is divided into horizontal slices of circular cross
section. Since the equations are linear in the particle concentration, the
solutions for each slice are superimposed to produce the final solution.
The individual solutions are obtained by transform methods. Specifically,
we consider moments of the particle concentration function $C(x,y,z,t)$, viz.,

$$T_{pq} \equiv \iint_{-\infty}^{\infty} x^p y^q \, C \, dx dy \qquad (3\text{-}7)$$

where x is the coordinate in the windward direction. If the diffusion equation

$$\frac{\partial C}{\partial t} + \nabla \cdot \vec{\Gamma} = 0 \qquad , \qquad (3\text{-}8)$$

where $\vec{\Gamma}$ denotes the particle flux vector components

$$\Gamma_x = uC - D_x \frac{\partial C}{\partial x} \qquad , \qquad (3\text{-}9a)$$

$$\Gamma_y = - D_y \frac{\partial C}{\partial y} \qquad , \qquad (3\text{-}9b)$$

$$\Gamma_z = - v_g C - D_z \frac{\partial C}{\partial z} \qquad (3\text{-}9c)$$

(with u the z-dependent wind velocity; D_x, D_y, and D_z the z-dependent diffus-
ivities along x, y, and z directions; and v_g the particle terminal settling
velocity), is multiplied by appropriate powers of x and y and integrated over
all x and y, the moment equations are obtained:

$$\left(\frac{\partial}{\partial t} - \frac{\partial}{\partial z} D_z \frac{\partial}{\partial z} - v_g \frac{\partial}{\partial z} \right) T_{pq} = pu \, T_{p-1,q} + p(p-1)D_x T_{p-2,q}$$

$$+ \, q(q-1)D_y T_{p,q-2} \equiv R_{pq} \qquad . \qquad (3\text{-}10)$$

43

The first several moments, respectively, describe: the mass distribution of dust in the cloud as a function of height z and time t ($p = q = 0$); its mean along-wind (x) position ($p = 1$, $q = 0$); its mean cross-wind (y) position ($p = 0$, $q = 1$); its along-wind spread ($p = 2$, $q = 0$); and its cross-wind spread ($p = 0$, $q = 2$).

If variables are made dimensionless with respect to a length h equal to the height of release, a velocity $[D_z h/h]$, and a time $[h^2/D_z(h)]$, the equation for the zeroth moment T_{00}, subject to a diffusivity $D_z = D_z(h)z^n$, initial conditions

$$t = 0, \quad T_{00} = \frac{Q}{h^3} \delta(z-1) \tag{3-11}$$

and the boundary conditions

$$z = 0, \quad z^n(\partial T_{00}/\partial z) = 0 \tag{3-12a}$$

$$z \rightarrow \infty, \quad T_{00} \rightarrow 0 \quad , \tag{3-12b}$$

can be solved in closed form to obtain for $v_g = 0$

$$T_{00}(z,t) = \frac{Q}{h^3(2-n)} \frac{z^{(1-n)/2}}{t} \exp\left[-\frac{z^{2-n}+1}{(2-n)^2 t}\right] I_{(n-1)/(2-n)}\left[\frac{2z^{1-n/2}}{(2-n)^2 t}\right] \tag{3-13}$$

where $I_{(n-1)/(2-n)}$ denotes the modified Bessel function of the first kind of order $[(n-1)/(2-n)]$. If $v_g \neq 0$, a closed form expression for the zeroth moment may be obtained by heuristic matching of two asymptotic solutions obtained by the following process. The equation

$$\frac{\partial T_{00}}{\partial t} - \frac{\partial}{\partial z}\left[z^n \frac{\partial T_{00}}{\partial z} + \alpha T_{00}\right] = 0 \quad , \tag{3-14}$$

where $\alpha \equiv v_g h/D_z(h)$, is recast in terms of the independent variables

$$\xi \equiv z + \alpha t - 1 \quad , \qquad \tau \equiv t$$

to obtain

$$\frac{\partial T_{00}}{\partial \tau} - \frac{\partial}{\partial \xi}\left[(\xi - \alpha\tau + 1)^n \frac{\partial T_{00}}{\partial \xi}\right] = 0$$

which, in turn, may be approximated by

$$\frac{\partial T_{00}}{\partial \tau} - \frac{\partial}{\partial \xi}\left[(1 + \xi)^n \frac{\partial T_{00}}{\partial \xi}\right] = 0 \qquad (3\text{-}15a)$$

in $\xi \gg \alpha\tau$, and by

$$\frac{\partial T_{00}}{\partial \tau} - (1 - \alpha)^n \frac{\partial^2 T_{00}}{\partial \xi^2} = 0 \qquad (3\text{-}15b)$$

in $\xi \gg \alpha\tau$. The solution to Eq. (3-15a), subject to the initial and boundary conditions (Eqs. 3-11, 3-12a, 3-12b), is readily transposed from Eq. (3-13), viz.,

$$T_{00}^{(0)}(\xi,\tau) = \frac{Q}{h^3(2-n)} \frac{(\xi+1)^{(1-n)/2}}{\tau} \exp\left[-\frac{(\xi+1)^{2-n}+1}{(2-n)^2\tau}\right]$$

$$\times I_{(n-1)/(2-n)}\left[\frac{2(\xi+1)^{1-n/2}}{(2-n)^2\tau}\right] \qquad (3\text{-}16a)$$

The solution to Eq. (3-15b), subject to the initial condition Eq. (3-11), the requirement of boundedness as $\xi \rightarrow \pm \infty$, and the restriction $(1 - \alpha\tau) \geq 0$, takes the classical Laplace form

$$T_{00}^{(i)}(\xi,\tau) = \frac{Q}{h^3}\tilde{\tau}^{-1/2}\exp\left[-\frac{\xi^2}{4\tilde{\tau}}\right] \qquad (3\text{-}16b)$$

where $\tilde{\tau} \equiv \displaystyle\int_0^\tau (1 - \alpha\tau)^n \, d\tau$. A heuristic composite solution to Eq. (3-14), valid in $z \geq 0$ and $\tau \leq \alpha^{-1}$, may then be written as

45

$$T_{00}(\xi,\tau,\alpha) \;=\; f(\xi,\alpha\tau)\, T_{00}^{(1)}(\xi,\tau) \;+\; \Big[1 - f(\xi,\alpha\tau)\Big]\, T_{00}^{(0)}(\xi,\tau) \;, \qquad (3\text{-}17)$$

where $f(\xi,\alpha\tau)$ denotes a suitably selected weight function (see below) satisfying the requirements $f \to 0$ in $\xi \gg \alpha\tau$, $f \to 1$ in $\xi \ll \alpha\tau$.

A judicious choice of the function $f(\xi,\alpha\tau)$ is obtained upon a study of the exact solution of Eq. (3-14) for the special case $n = 1$, i.e., the case of neutral stratification, where the diffusivity varies linearly with the height z. In that case, the change of dependent variable

$$\widetilde{T}_{00}(z,t) \;\equiv\; z^{\alpha}\, T_{00}(z,t)$$

leads to the equation

$$z^{-\alpha}\, \frac{\partial \widetilde{T}_{00}}{\partial t} \;-\; \frac{\partial}{\partial z}\left[z^{1-\alpha}\, \frac{\partial \widetilde{T}_{00}}{\partial z} \right] \;=\; 0$$

with solution, subject to the initial and boundary conditions (3-11) and (3-12a,b),

$$\widetilde{T}_{00}(z,t) \;=\; z^{\alpha} T_{00}(z,t) \;=\; \frac{Q}{h^{3}}\, \frac{z^{\alpha/2}}{t}\, \exp\left[-\frac{z+1}{t} \right] I_{\alpha}\left[\frac{2z^{1/2}}{t} \right] \;. \qquad (3\text{-}18)$$

Whereas the solutions given by Eqs. (3-16a,b) are also known, the weight function $f(\zeta,\alpha\tau)$ is readily determined upon comparison of Eqs. (3-17) and (3-18). If this result, strictly obtained for $n = 1$, is adopted throughout the practical range of values $0 < n \leqslant 4/3$ associated with stable to unstable stratifications, the closed form solution Eq. (3-17) for the zeroth moment becomes completely defined. The availability of this solution substantively simplifies the determination of the higher moments along the lines presented below.

Returning to Eq. (3-10), we note that the same differential operator appears in the equations for all the moments. However, while the equation for T_{00} is homogeneous, those for the higher moments include known forcing functions R_{pq}. Whereas the initial conditions are: $t = 0$, $T_{00} \propto \delta(z - 1)$,

and $T_{pq} = 0$; the solution Eq. (3-17) for T_{00} provides the Green's function required to construct solutions for the higher moments by superposition. Specifically, if we let

$$G(\xi,\xi',\tau,\tau',\alpha) \equiv f[\xi-\xi', \alpha(\tau-\tau')] [\tau-\tau']^{1/2} \exp\left[-\frac{(\xi-\xi')^2}{4(\tau-\tau')}\right]$$

$$+ \left\{1 - f[\xi-\xi', \alpha(\tau-\tau')]\right\} \frac{[(\xi+1)(\xi'+1)]^{(1-n)/2}}{(2-n)(\tau-\tau')} \exp\left[-\frac{(\xi+1)^{2-n} + (\xi'+1)^{2-n}}{(2-n)^2 (\tau-\tau')}\right]$$

$$\times I_{(n-1)/(2-n)}\left[\frac{2(\xi+1)^{1-n/2}(\xi'+1)^{1-n/2}}{(2-n)^2 (\tau-\tau')}\right] \quad , \tag{3-19}$$

then, the solution for the general moment becomes

$$T_{p,q}(\xi,\tau) = \int_{\alpha\tau^{-1}}^{\infty} d\xi' \int_{0}^{\tau} R_{pq}(\xi',\tau') \, G(\xi,\xi',\tau,\tau',\alpha) \, d\tau' \quad , \tag{3-20}$$

which can be readily evaluated by numerical integration.

A matrix of solutions (3-20) covering the ranges of the parameters n and α associated with Pasquill stability categories A through F (see Appendix B) and dust particle sizes $D \leq 100$ μm have been evaluated. The results in tabular form are included in the DIRTRAN-I code together with interpolation routines which permit determination of the solutions for intermediate values of the parameters (Ref. 1). By this process, the calculation of the dust concentration within a given dust size bin at a prescribed location and time achieves the same simplicity as the evaluation of a Gaussian. Predictions of this model are compared with data in Section 5.

4. OPTICAL PROPERTIES OF DUST CLOUDS

The DIRTRAN model calculates the transmittance through a dust cloud according to the relation

$$T = \exp\left[-\int_0^\ell \alpha C d\ell \right] \tag{4-1}$$

where ℓ is the thickness of the cloud along the line of sight, and α is the mass extinction coefficient which depends on wavelength, particle size distribution, and material. The diffusion calculations described in Section 3 yield the integral

$$I = \int_0^\ell C d\ell = \overline{C}\ell \tag{4-2}$$

where $\overline{C}$ is the average concentration along the line of sight. The model approximates Eq. (4-1) by the relation

$$T = \exp(-\overline{\alpha}\,\overline{C}\ell) \tag{4-3}$$

where $\overline{\alpha}$ is estimated from laboratory data as shown in Fig. 20 (Ref. 18) and inferred from ratios of transmittances in field experiments (Refs. 7, 19, 20). In principle, if the chemical composition and associated refractive index of the dust material were given together with the dust particle distribution function, Mie theory could be used to systematically calculate $\overline{\alpha}$ (ignoring the problem of particle nonsphericity). In fact, these calculations have been carried out parametrically by Jennings et al. (Ref. 21). The salient results, shown in Fig. 21, indicate that the extreme variation in extinction coefficient for soil-like materials as a result of refractive index variations due to different chemical constituents is:
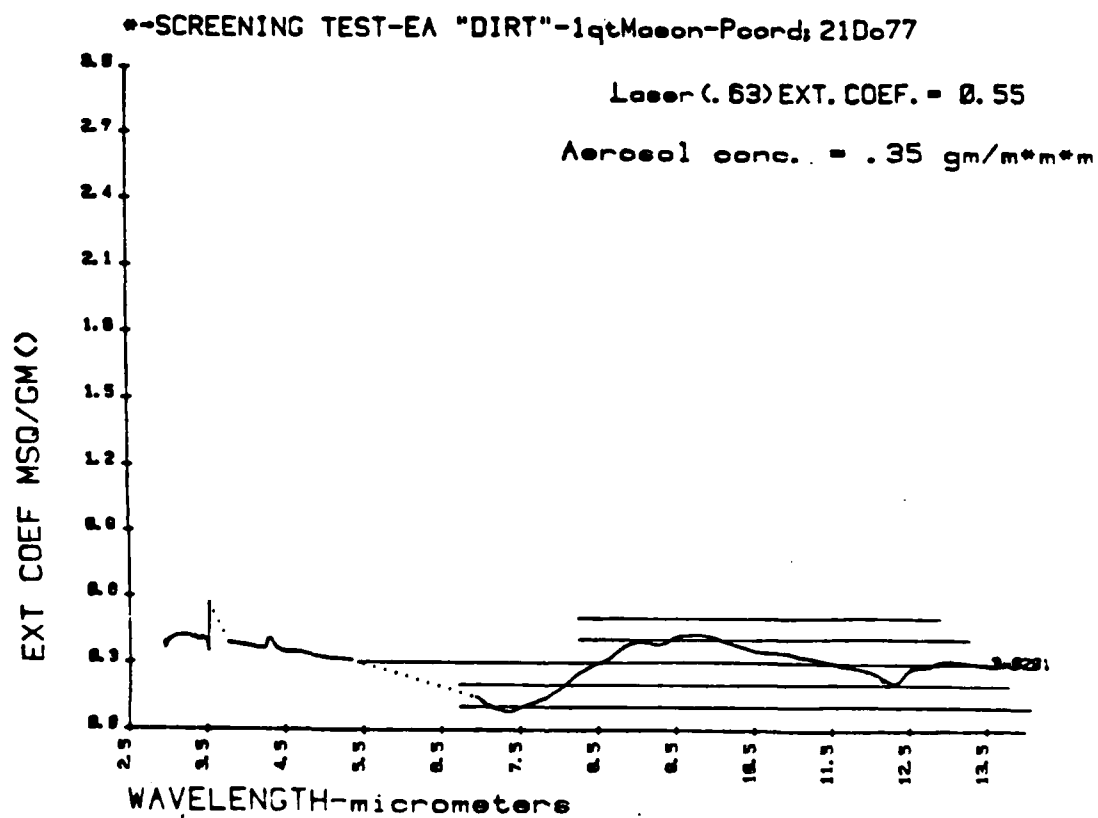
Figure 20. Mass Extinction Coefficient of Edgewood
Arsenal "Dust" (Ref. 18)
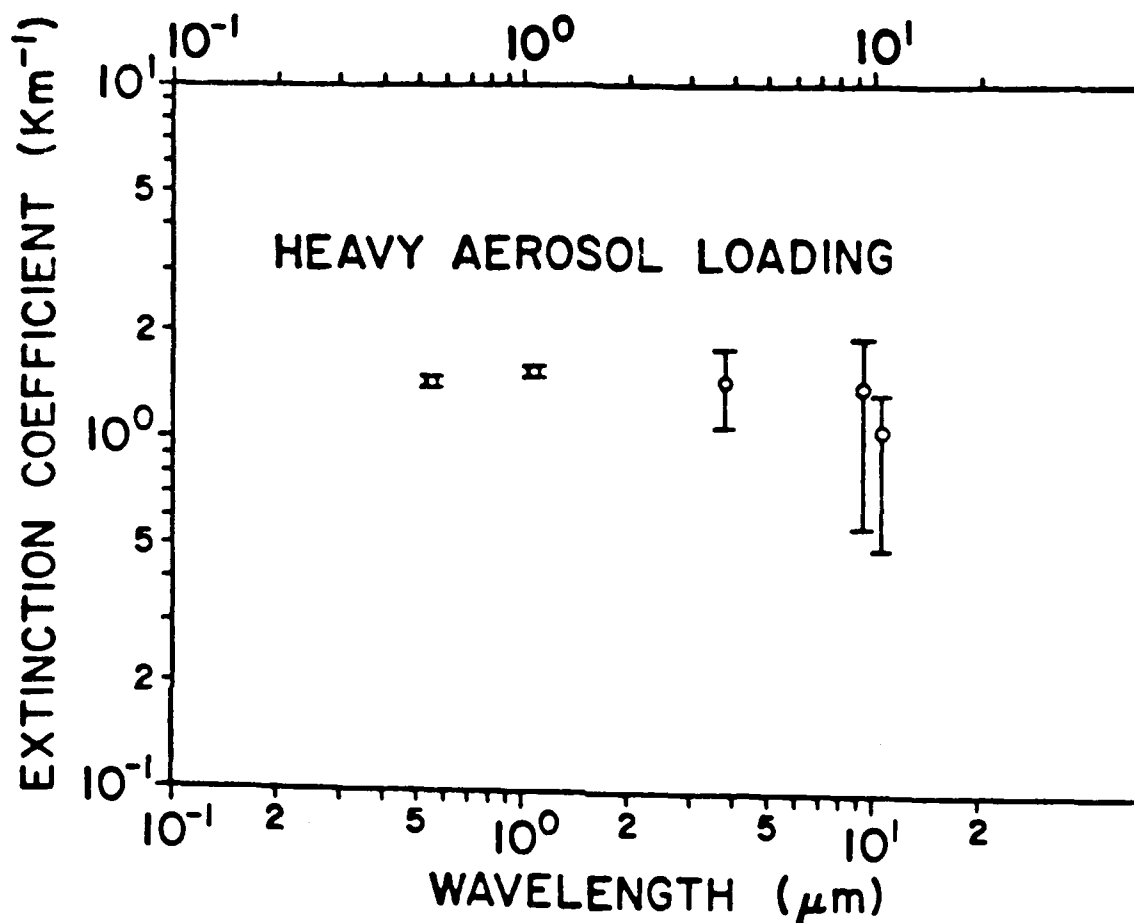
Figure 21. Aerosol Extinction Coefficient vs Wavelength for Aerosol
Mass Loading (1.5×10^{-2} g/m^3) Characterized by Bimodal
Particle Size Distributions With Geometric Radii 0.5 and
15 µm and Standard Deviation 2.25 and 1.6 respectively.
The circles indicate extinction values for typical refrac-
tive indexes, and the error bars indicate the extreme ex-
tinction values due to refractive index variations
(Ref. 21).

50

(a) negligible (<5%) for wavelengths $\lambda \lesssim 1 \ \mu m$

(b) $\pm 30\%$ for $\lambda \approx 4 \ \mu m$

(c) $\pm 50\%$ for $\lambda \approx 10 \ \mu m$. .

Jenning's calculations for the variation in relative extinction coefficient versus wavelength are also supported by DIRT I, Graf II, and Ft. Sill Dust/ Debris measurements, which, within $\pm 30\%$ scatter, indicate the relative values shown in Table 4-1. In view of the uncertainties in soil comminution/agglomeration raised in Section 2 and quantified in Section 5, it was deemed appropriate at the present to adopt in the DIRTRAN model these average values of $\bar{\alpha}$.

Table 4-1. Relative Mass Extinction Coefficients

$\lambda (\mu m)$	$0.4-0.7$[*]	$0.8-1.1$	$3.5-4.0$	$8.5-12$	$2100-3200$[**]
$\alpha (m^2/g)$	1	0.9	0.7	0.5	7×10^{-4}

[*] $\bar{\alpha}_{visible} = 550 \ m^2/kg$ (Ref. 18)

[**] These values are for Rayleigh regime particles (relative to mm waves) as determined from the asymptotic attenuation level ($t > 15$ sec) observed in the DIRT I C-1 event.

A divergence exists between the extinction coefficients extracted from Jennings calculations, viz., $\alpha = k/C$ (where k is given by Fig. 21 and $C = 1.5 \times 10^{-2} \ g/m^3$), and those reported in Fig. 20. The latter values are approximately a factor 5 higher. Although no information concerning the particle size distribution function is reported in Ref. 18, the Fig. 20 data were adopted in the DIRTRAN model because they represent actual measurements of a real soil sample.

5. DATA ANALYSIS, MODEL VALIDATION, AND DISCUSSION

The capability of the buoyantly rising cloud model in the DIRTRAN code is illustrated by the comparisons shown in Figs. 22, 23, and 24 for data from the DIRT I test series. Test B-2 (Fig. 22) involved a 3 x 1 array of 6.8 kg bare charges; Test E-3 (Fig. 23) involved a 3 x 4 array of 6.8 kg charges (155 mm HE projectiles); and Test C-1 (Fig. 24) involved a 7 x 20 array of 6.8 kg bare charges. The atmospheric conditions in the three cases are respectively consistent with Pasquill categories E, C, and E. The departure between theory and observations for C-1 at 80 seconds after detonation is due to the presence of a temperature inversion (determined by acoustic sounder, Ref. 22) at an altitude of 140m. The strong sensitivity of the predictions to stability category is also shown in Fig. 23. Thus, the accuracy required in near-ground meteorological measurements must be such as to provide significant distinctions between vertical temperature and wind velocity differences associated with different stability regimes.

The capabilities of the wind-controlled diffusion model are exhibited in Figs. 25 and 26 for events B2 and C1. The wind velocity and direction (relative to the line of sight) for Event B2 are 1.3 m/s and $45°$, respectively; for Event C-1, they are 1.3 m/s and $9°$. It should be noted that these wind velocities represent the average of the 5-minute average readings of the north and south meteorological station sites* as reported in Ref. 7. The wind directions constitute intermediate values between the 5 minute average readings at the two sites, readings which differ by approximately $100°$ in both events. Because calculations show that the time for initial transmission recovery is controlled by wind advection of the dust cloud perpendicular to the line of sight, the importance of careful meteorological measurements as near as possible to the test area is emphasized. The time average of these measurements should also be made on time scales smaller than or, at worst,

---

*These sites were each located one kilometer from the test area.

COMPARISON OF DIRTRAN MODEL
PREDICTIONS WITH CLOUD HEIGHT DATA

(SOURCE: DIRT I TEST, OCTOBER 1978)
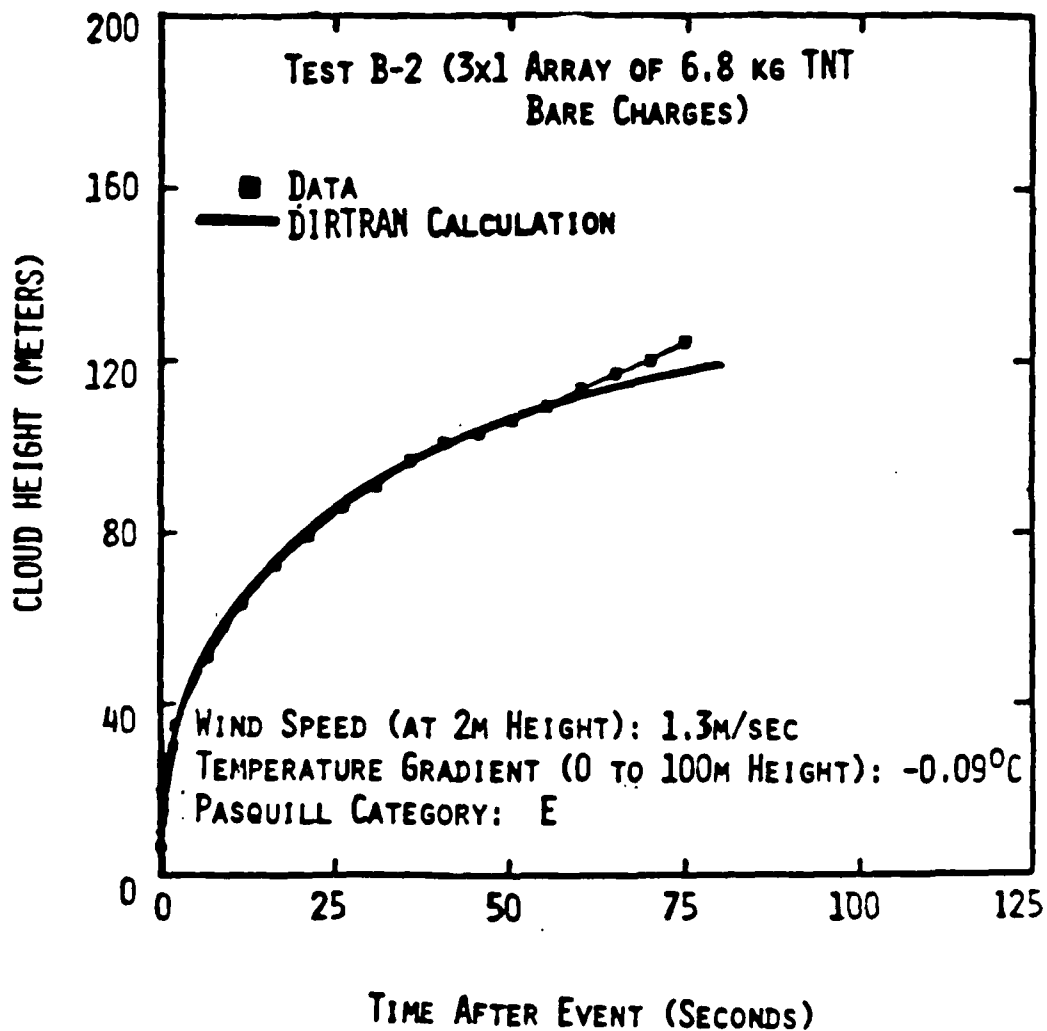
Figure 22. Comparison of DIRTRAN Model Cloud Height Versus Time
Predictions with Data From Event B-2 (three 6.8 kg
bare charges) of the DIRT I Test Series.
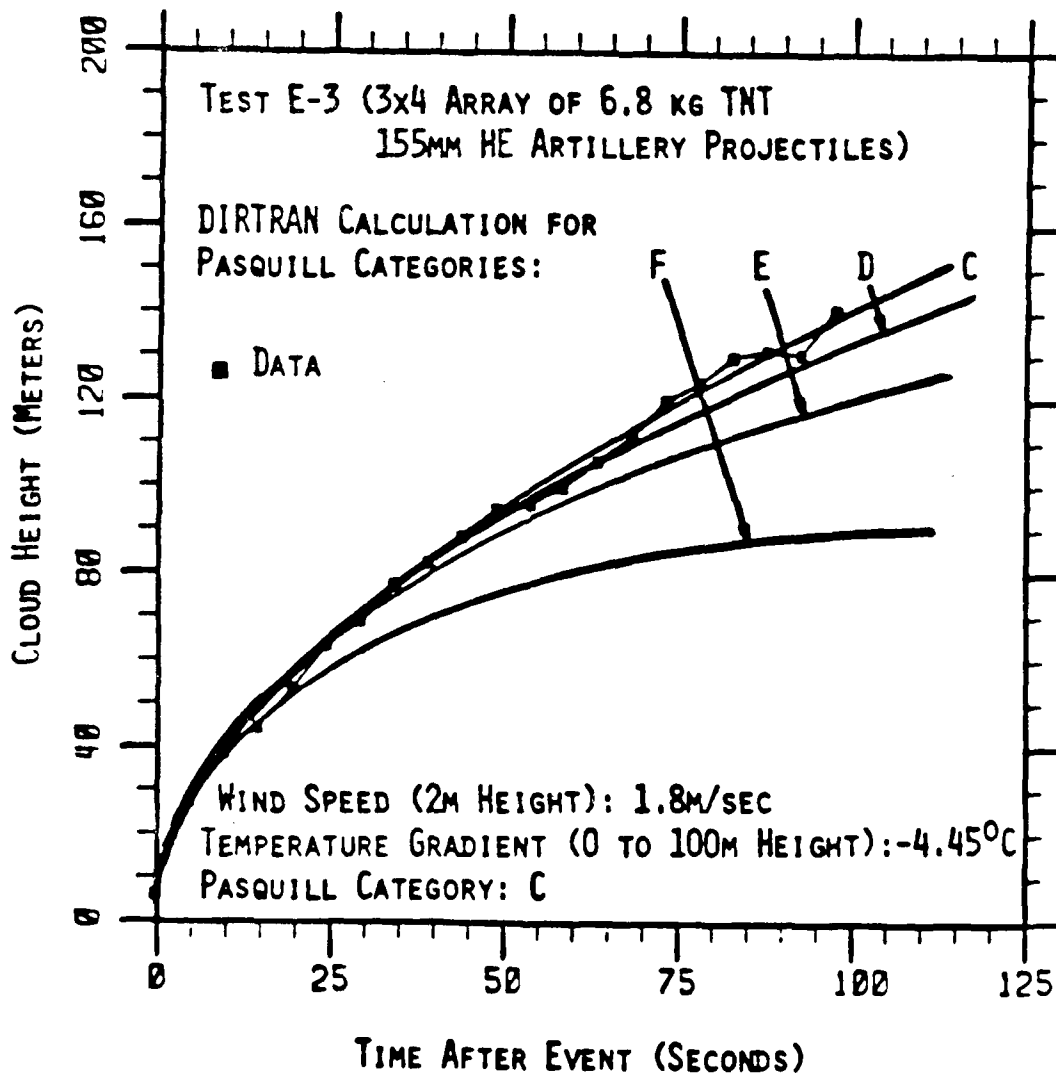
Figure 23. Comparison of DIRTRAN Model Cloud Height Predictions with
DIRT I Data for Event E-3 (twelve statically detonated
155 mm HE artillery projectiles). Note sensitivity of
calculations of cloud height to atmospheric stability
category.

COMPARISON OF DIRTRAN MODEL
PREDICTIONS WITH CLOUD HEIGHT DATA

(SOURCE: DIRT I TEST, OCTOBER 1978)
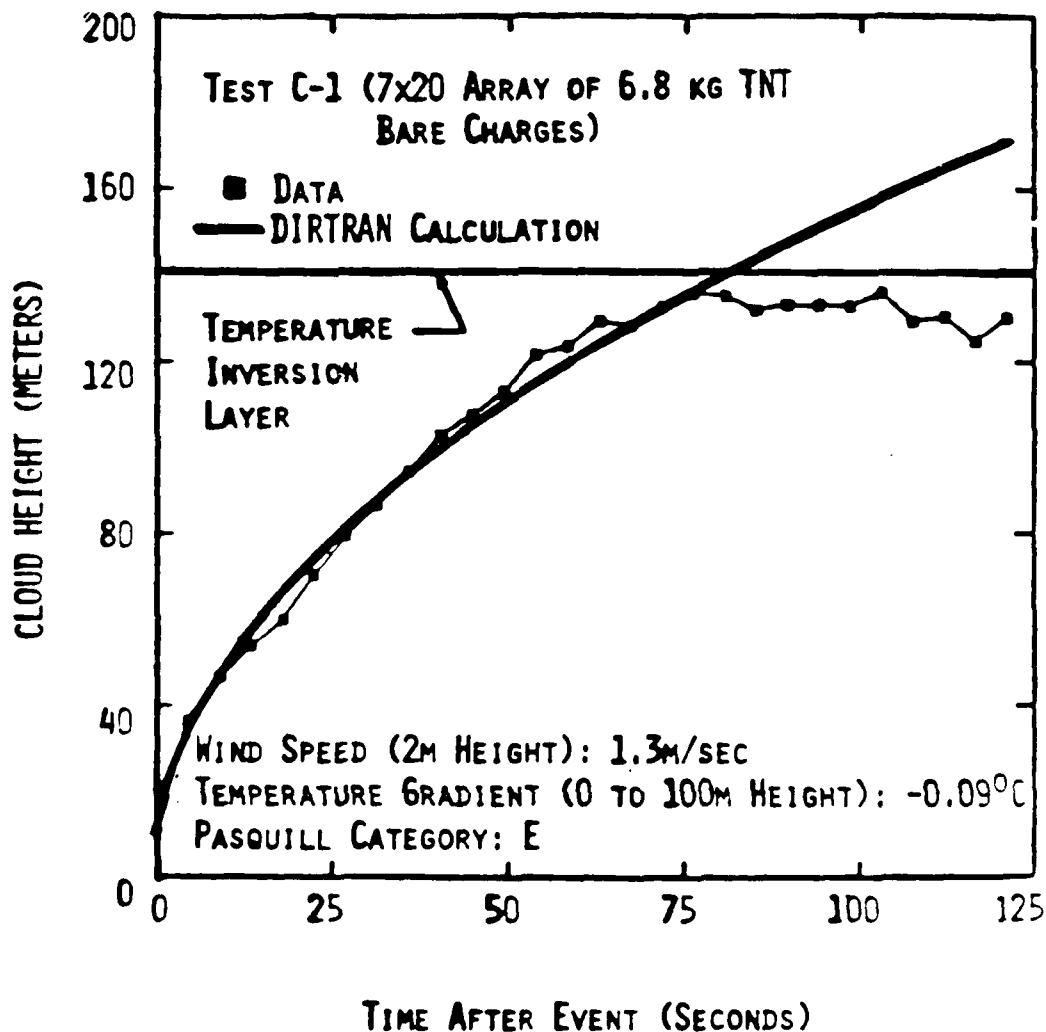
Figure 24. Comparison of DIRTRAN Model Cloud Height Predictions with
DIRT I Data for Event C-1 (140 6.8 kg bare charges).
The existence of a temperature inversion layer at 140m
(determined by acoustic sounder, Ref. 22) results in
departure of model predictions from actual cloud height.

55

Figure 25. Comparison of DIRTRAN Model Optical Transmission Predictions
with DIRT I Data for Event B-2. Note intermediate recovery
of transmission due to incomplete merging of dust skirts
caused by the individual explosions at the time when the
midway point between the two clouds is advected across
the line of sight.

EVENT C—1

78 OCT 05   0711 MDT

NRL Data (Preliminary)
------- 10.35μ
———— 0.55μ

DIRTRAN Calculation Inputs
Pasquill Category: E
Windspeed (2m Height): 1.3m/sec
Wind Direction (relative to LOS): 9°
Charge Size: 6.8 kg
Charge Array: 7 x 20

DIRTRAN (10 μm)

DIRTRAN (0.55 μm)

Figure 26. Comparison of DIRTRAN Model Optical Transmission Predictions
with DIRT I Data for Event C-1 for Which Transmission
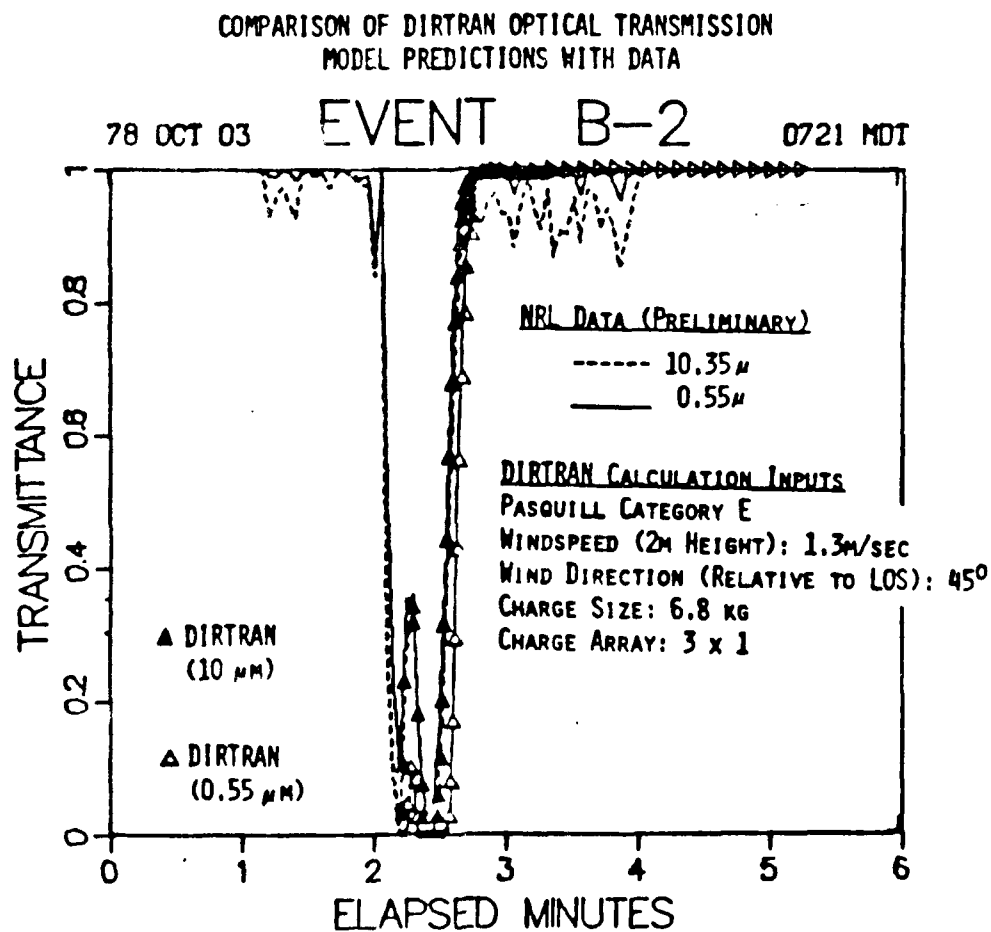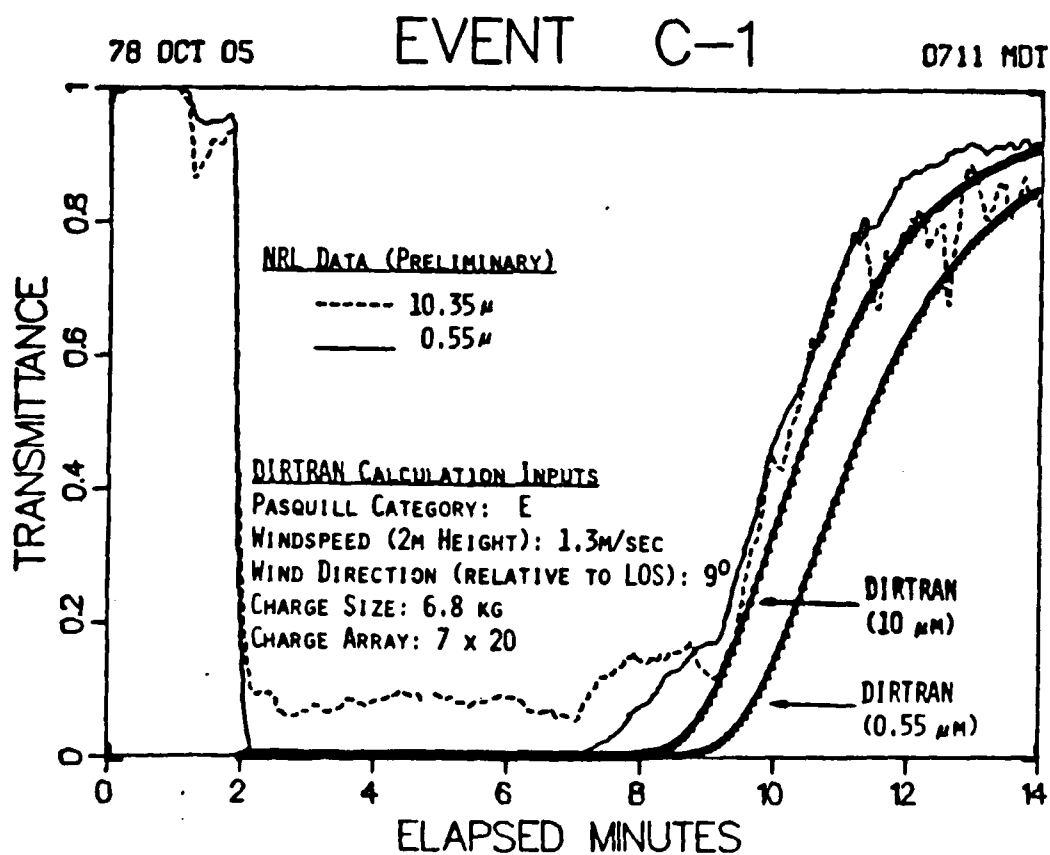Recovery Occurs Only After Long Times After Detonation
(>10 Minutes).

equal to the obscuration times. Meteorological measurements should also be
taken at different sites along the entire length of the line of sight. The
latter requirement is manifested by the optical data for cases B4, B5, B6,
B7, and D1 where the "cloud folded back" over the line of sight (Ref. 7).

Additional points of interest in Figs. 25 and 26 include the intermediate
transmission recovery for event B2 (Fig. 25). This is due to incomplete merg-
ing of the dust skirts caused by the individual explosions at the time when
the midway point between two adjacent clouds was advected across the line of
sight. The existence and magnitude of this intermediate recovery can be
reproduced in calculations only by allowing a drastic reduction (quantified
by an agglomeration parameter approximately equal to seven) in the concentra-
tion of optically active particles predicted by crater volume calculations
and dry-soil sieve analyses. Such reduction can be explained by soil agglomer-
ation under dynamic loading (cf. Section 2). Two additional results support
this view: (1) the agreement between calculations and observations for the
final transmission recovery along the near-ground line-of-sight (Fig. 26);
(2) the apparent dissipation of the buoyant cloud for times t ~ 80 sec after
detonation indicated in Fig. 22. Whereas only one comminution/agglomeration
parameter has been introduced, the congruence between predicted time-dependent
transmission across two distinct clouds suggests that the effect in question
is a real one and the attendant estimate justifiable. Given the magnitude of
the parameter, this constitutes the dominant influence upon optical properties
of dust clouds produced by explosions in a given soil. To be sure, the
agglomeration effect extracted in the B2 event also provides good agreement
between calculations and observations for event C1 (Fig. 26). Noteworthy in
the latter case is also the success of the model at very long times, i.e.,
the prediction of transmission recovery approximately ten minutes after
detonation.

The large agglomeration effect exhibited in the DIRT I data analysis
cannot be blindly extrapolated to other soils. It can only be conjectured
that its influence on dust optical properties will remain large for other

soils. However, quantification of the effect remains dependent on systematic soil testing under conditions of (explosive) dynamic loading. It is worth repeating that an interesting approach may be provided by small scale experiments with reduced charge sizes which yield partially transmitting dust clouds at all times subsequent to detonation. Optical diagnostics at several wavelengths and lines of sight could be applied to such clouds to obtain spatially and temporally resolved data throughout their history.

6. SUMMARY/CONCLUSIONS

A model (DIRTRAN) descriptive of time/space dependent optical properties of explosion-generated dust clouds has been developed. This model includes three components: a dust source term, atmospheric diffusion, and optical transmission. Data analysis indicates that, for a given soil, the greatest uncertainties lie in the determination of soil comminution/agglomeration under the dynamic loading produced by explosions. When an empirical parameter descriptive of this effect is employed, the model predicts cloud optical properties which compare favorably with experiments under a variety of explosion patterns, charge types, and atmospheric conditions. A computer code (DIRTRAN-I) which embodies this model has been delivered to the Army Atmospheric Sciences Laboratory for inclusion in the Electro-Optics Systems Atmospheric Effects Library.

7. REFERENCES

1. D. Dvore, "DIRTRAN-I User's Manual," Aerodyne Doc. No. ARI-RR-178.1, 20 September 1979.

2. D.J. Roddy, R.O. Pepin, and R.B. Merrill, eds., Impact and Explosion Cratering (Pergamon, New York 1977).

3. B.G. Killian and L.S. Germain, "Scaling of Cratering Experiments -- An Analytical and Heuristic Approach to the Phenomenology," pp. 1165-1190, D.J. Roddy et al., eds., op. cit.

4. C.F. Knowles and H.L. Brode, "The Theory of Cratering Phenomena, An Overview," pp. 869-895, D.J. Roddy et al., eds., op. cit.

5. "Cratering from High Explosive Charges: Analysis of Crater Data," Tech. Rpt. No. 2-547, Report 2, June 1961, U.S. Army Engineer Waterways Experiment Station, Corps of Engineers, Vicksburg, Miss.

6. L. Leftin and J. Ebersole, "Analytic Expressions for Crater Dimension Data from the Army Waterways Experiment Station, Corps of Engineers," Aerodyne Doc. No. ARI-LR-80.1; also, J. Ebersole et al., "Battlefield-Induced Aerosol Contaminants: An Assessment of Obscuration Yields" (Report in preparation).

7. J. Lindberg, ed., "Measured Effects of Battlefield Dust and Smoke on Visible, Infrared, and Millimeter Wavelength Propagation: A Preliminary Report on the Dusty Infrared Test-I (DIRT-I)," Rpt. ASL-TR-0021, January 1979, Atmospheric Sciences Laboratory, White Sands Missile Range, NM 88002.

8. C.A. Miller, "Terrain Characteristics at DIRT-I Test Site, White Sands Missile Range, New Mexico," Tech. Rpt., U.S. Army Engineer Waterways Experiment Station, Vicksburg, Miss., December 1978.

9. J. Lundien, "Graf II Realistic Battlefield Sensor Trials," Tech. Rpt., U.S. Army Engineer Waterways Experiment Station, Vicksburg, Miss., March 1979.

10. W.R. Seebaugh, "A Dynamic Crater Ejecta Model," pp. 1043-1056, D.J. Roddy et al., eds., op. cit.

11. J.F. Ebersole, R. Vaglio-Laurin, D.S. Dvore, and M. Martinez-Sanchez, "Analysis and Modeling of the DIRT I and Graf II Battlefield Dust Obscuration Data," Final Tech. Rpt., Aerodyne Doc. No. ARI-RR-168, June 1979

12. J. Thompson, "S-Shock Code," Report GE75TMP-14, General Electric - TEMPO, March 1975.

13. M.A. Cook, The Science of Explosives (American Chemical Society, Huntington, NY, 1971).

14. R.B. Chavez, "Fixed-Camera Data, Dusty Infrared Test I, 2 October 1978 thru 14 October 1978," Final Data Rpt. No. 37,179, Physical Science Laboratory, New Mexico State University, Las Cruces, NM, 17 July 1979.

15. G. Blackman and L. Duncan, Army Atmospheric Sciences Laboratory, private communication, August 1979.

16. B.R. Morton, G. Taylor, and J.S. Turner, "Turbulent Gravitational Convection from Maintained and Instantaneous Sources," Proc. Roy. Soc. A, $\underline{234}$, 1-23, 1956.

17. J.S. Turner, "Buoyant Plumes and Thermals," Ann. Rev. Fluid Mech. $\underline{1}$, 29-44 (1969).

18. G. Holst, Army Chemical Systems Laboratory, private communication, April 1978.

19. L. Obert, Army Night Vision & Electro-Optics Laboratory, Graf II-Winter transmission data, private communication, March 1979.

20. "Dust/Debris Test Conducted at Fort Sill, Oklahoma by Dugway Proving Ground," Final Test Rpt. DPG-FR-78-313, Vols. I and II, Sept. 1978.

21. S.G. Jennings, R.G. Pinnick, and H.J. Auverman, "Effects of Particulate Refractive Index and Particle Size Distribution on Atmospheric Extinction and Absorption for Visible through Middle IR Wavelengths," Appl. Opt. $\underline{17}$, 3922-3929 (1978).

22. R. Olsen, Army Atmospheric Sciences Laboratory, private communication, August 1979.

23. F. Pasquill, Atmospheric Diffusion, 2nd ed. (Wiley, New York, 1974).

24. K.W. Ragland and R.L. Dennis, "Point Source Atmospheric Diffusion Model with Variable Wind and Diffusivity Profiles," Atm. Environment, $\underline{9}$ 175-189 (1975).

25. J.H. Seinfeld, Air Pollution (McGraw-Hill, New York, 1975).

APPENDIX A
AERODYNAMIC ARREST OF PARTICLES

The retardation of a spherical particle of radius r by aerodynamic drag is described by[*]

$$m \frac{dV}{dt} \cong - \frac{1}{2} \rho_a V^2 C_D A \qquad (A-1)$$

where

$\quad$ m $\quad$ = mass of particle = $\frac{4}{3} \pi r^3 \rho_p$

$\quad \rho_a$ $\quad$ = air density

$\quad \rho_p$ $\quad$ = particle density

$\quad$ V $\quad$ = particle velocity

$\quad C_D$ $\quad$ = drag coefficient

$\quad$ A $\quad$ = cross-sectional area of particle = πr^2

For Reynolds number $Re = 2rV/\nu_a \leq 50$ (where ν_a is the kinematic viscosity of air), the drag coefficient may be approximated by $C_D = 24/Re$, while, for $50 \leq Re \leq 3 \times 10^5$, $C_D \cong 0.47$. Eq. (A-1) can be readily integrated to yield for the constant-drag-coefficient regime ($C_D = 0.47$)

$$\frac{1}{V_f} - \frac{1}{V_i} = \frac{3}{8} \frac{\rho_a}{\rho_p} \frac{C_D}{r} t \equiv \frac{at}{r} \qquad (A-2)$$

where

$\quad V_f$ $\quad$ = velocity at time t

$\quad V_i$ $\quad$ = initial velocity at t = 0

$\quad$ a $\quad$ = constant = $3\rho_a C_D / 8\rho_p$

---

[*] We have neglected the inertia terms of the fluid since $\rho_a/\rho_p \sim 10^{-3}$.

and for the Stoke's Law drag regime ($C_D = 24/Re$)

$$\ln \frac{V_f}{V_i} = -\frac{9}{2} \frac{\rho_a \nu_a}{\rho_p} \frac{t}{r^2} \equiv \frac{-bt}{r^2} \tag{A-3}$$

where

$$b = \text{constant} = 9\rho_a \nu_a / 2\rho_p$$

The distances traveled by the particle having initial velocity V_i during the time interval$t$ is, for the constant-drag-coefficient regime ($3 \times 10^5 \geq Re \geq 50$),

$$s = \frac{r}{a} \ln \left(1 + \frac{aV_i t}{r}\right) \tag{A-4}$$

$$= \frac{r}{a} \ln \left(\frac{V_i}{V_f}\right) \tag{A-5}$$

and, for $R \leq 50$,

$$s = \frac{r^2}{b} V_i \left[1 - \exp(-bt/r^2)\right] \tag{A-6}$$

$$= \frac{r^2}{b} (V_i - V_f) \tag{A-7}$$

The total distance traveled s_T and total time t_T for a particle to come to rest are calculated as follows. Particles with radius r and initial velocity V_i such that $3 \times 10^5 \geq Re \geq 50$ are retarded according to Eqs. (A-2) and (A-4) until $Re = 2rV_f/\nu_a = 50$ or

$$V_f = \frac{25\nu_a}{r} \quad . \tag{A-8}$$

From Eq. (A-5), one then computes the distance s_1 traveled in this phase of constant-drag-coefficient as

$$s_1 = \frac{r}{a} \ln \left(\frac{V_i r}{25\nu_a}\right) \tag{A-9}$$

64

From Eq. (A-2), the time t_1 to travel this distance is

$$t_1 = \frac{r}{a}\left(\frac{r}{25\nu_a} - \frac{1}{V_1}\right) \qquad \text{(A-10)}$$

After this point in time, V_f in Eq. (A-8) becomes the initial velocity for the Stoke"s Law regime (Re $\leq$ 50), in which the distance traveled s_2 and time t_2 to reduce the velocity to $V_f e^{-3}$ can be calculated from Eqs. (A-6) and (A-3) respectively, viz.,

$$s_2 = \frac{25\nu_a r}{b} \qquad \text{(A-11)}$$

and

$$t_2 = \frac{3r^2}{b} \qquad \text{(A-12)}$$

Figures A-1 and A-2 show parametric curves of the total distance s_T and time of arrest t_T given by

$$s_T = s_1 + s_2 \qquad \text{(A-13)}$$

$$t_T = t_1 + t_2 \qquad \text{(A-14)}$$

for $\nu_a = 0.15$ cm^2/sec, $\rho_a = 1.2 \times 10^{-3}$ g/cm^3, and $\rho_p = 2.5$ g/cm^3. The range of initial velocities V_1 have been chosen in accordance with Ref. 10.
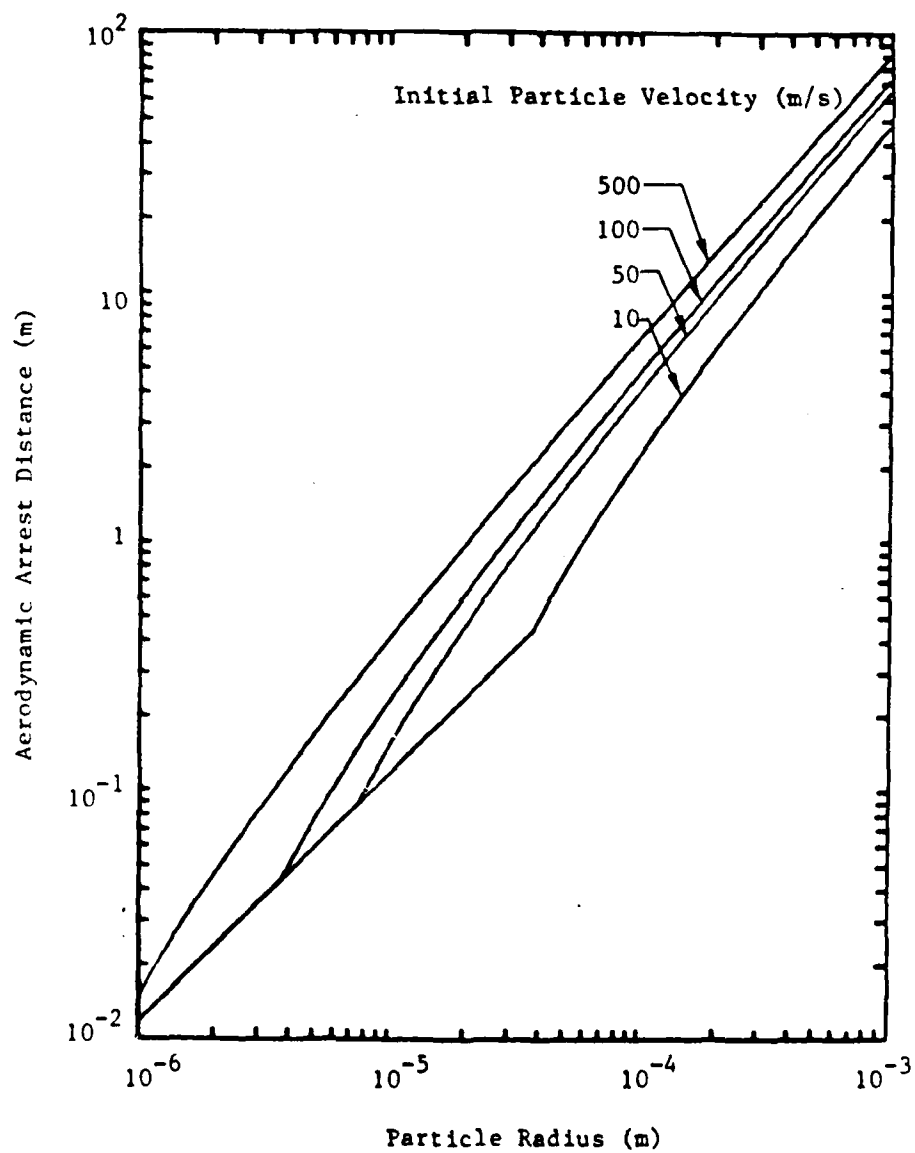
65

Figure A-1. Aerodynamic Arrest Distance Versus Particle
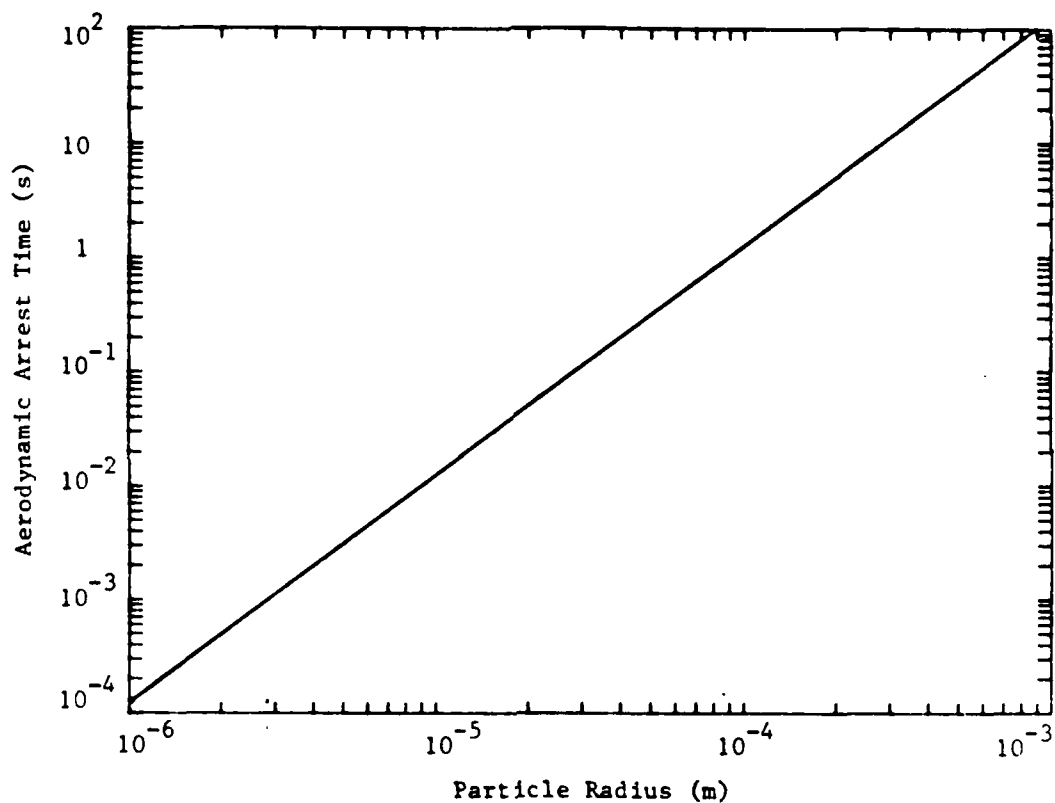Radius for Four Initial Velocities

Figure A-2. Aerodynamic Arrest Time Versus Particle Radius
for Initial Velocities of 10, 50, 100, and
500 m/s. (Curves are essentially identical
for these range of radii and initial velocities.)

67

APPENDIX B

DESCRIPTION OF THE ATMOSPHERIC BOUNDARY LAYER STRUCTURE

Attention is restricted to the constant stress layer where the wind velocity field remains planar. Following classical notation (Ref. 22), the Monin-Obukhov length L is defined as

$$L = \frac{\Theta u_*^2}{k^2 g T_*} \tag{B-1}$$

The profiles of wind velocity $u(z)$ and potential temperature $\Theta(z)$ for unstable stratification and $z \leq -2L$ are described by

$$\left. \begin{aligned}
u(z) &= \frac{u_*}{k} \left[\ln \left(\frac{z}{z_0} \right) - \Psi_M \left(\frac{z}{L} \right) \right] \\
\Theta(z) - \Theta(0) &= T_* \left[\ln \left(\frac{z}{z_0} \right) - \Psi_H \left(\frac{z}{L} \right) \right]
\end{aligned} \right\} \tag{B-2}$$

where

$$\Psi_M = -2 \left[\ln \left(\frac{S+1}{2} \right) + \frac{1}{2} \ln \left(\frac{S^2+1}{2} \right) - \tan^{-1}(S) + \frac{\pi}{4} \right] \tag{B-3}$$

$$\Psi_H = -2 \ln \left(\frac{S^2+1}{S} \right) \tag{B-4}$$

$$S = \left(1 - 16 \frac{z}{L} \right)^{1/4} \tag{B-5}$$

For unstable stratification and $z \geq -2L$, the profiles are

$$\left. \begin{aligned}
u(z) &= u_0 - 0.95 \, u_* \, |L|^{1/3} \, z^{-1/3} \, k^{-1} \\
\Theta(z) - \Theta(0) &= T_0 - 0.95 \, T_* \, |L|^{1/3} \, z^{-1/3}
\end{aligned} \right\} \tag{B-6}$$

68

where

$$u_o = \frac{u_*}{k} \left[\ell n \left(\frac{-2L}{z_o} \right) - \Psi_M(-2) + 0.75 \right] \tag{B-7}$$

$$T_o = T_* \left[\ell n \left(\frac{-2L}{z_o} \right) - \Psi_H(-2) + 0.75 \right] \tag{B-8}$$

For neutral stratification, the wind velocity profile is described by

$$u(z) = \frac{u_*}{k} \ell n \left(\frac{z}{z_o} \right) \tag{B-9}$$

For stable stratification, the wind velocity and potential temperature profiles are described by Eq. (B-2) with

$$\Psi_M = -7 \frac{z}{L} \tag{B-10}$$

$$\Psi_H = -11 \frac{z}{L} \tag{B-11}$$

for $z \leq 1.5L$, and by

$$\left. \begin{array}{l} u(z) = u_o + \dfrac{10u_* z}{kL} \\[2em] \Theta(z) - \Theta(0) = T_o + 10T_* \dfrac{z}{L} \end{array} \right\} \tag{B-12}$$

with

$$u_o = \frac{u_*}{k} \left[\ell n \left(\frac{1.5L}{z_o} \right) - \Psi_M(1.5) - 15 \right] \tag{B-13}$$

$$T_o = T_* \left[\ell n \left(\frac{1.5L}{z_o} \right) - \Psi_H(1.5) - 15 \right] \tag{B-14}$$

for $z \geq 1.5L$.

69

In all cases, the momentum and temperature diffusivities in the z direction are calculated from the definitions

$$D_{zM} = \frac{u_*^2}{(du/dz)} \qquad (B-15)$$

$$D_{z\Theta} = \frac{ku_*T_*}{(d\Theta/dz)} \qquad (B-16)$$

with du/dz and $d\Theta/dz$ determined consistent with the profiles given above. In accordance with Ref. 24, the corresponding diffusivities in the horizontal directions, D_{xM} and D_{yM}, are set equal to $5D_{zM}$, $6D_{zM}$, and $2D_{zM}$ for neutral, stable, and unstable stratifications respectively.

If wind and temperature measurements are given at two heights, the DIRTRAN-I code inverts the wind velocity and potential temperature profiles listed above to calculate case by case the quantities u_*, T_*, z_o, and L. Upon this determination, the wind velocity and potential temperature at any other height z are calculated from the same profiles. If wind velocity and temperature are measured at only one height, the DIRTRAN-I code requires that Pasquill stability category (A through F) (Ref. 22) and roughness height z_o be prescribed before the wind velocity and potential temperature profiles can be determined. With each stability category, there is associated a specific value of the Monin-Obukhov length in accord with Table B-1 (Refs. 22 and 25).

TABLE B-1

Monin-Obukhov Length vs Pasquill Stability Category*

Category	L (meters)
A	-2.5
B	-4.5
C	-13.5
D	1000
E	55
F	21.5

*Refs. 23, 25.

70